

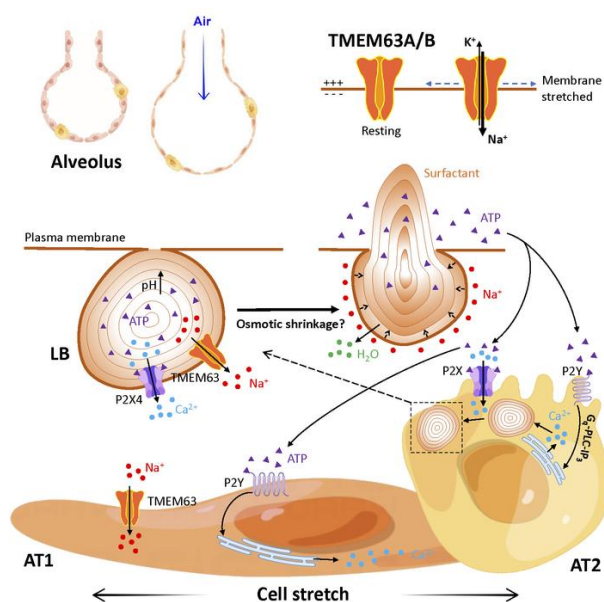
Mechanosensitive channels TMEM63A and TMEM63B mediate lung inflation-induced surfactant secretion

Gui-Lan Chen, ... , Jin Zhang, Bo Zeng

J Clin Invest. 2023. <https://doi.org/10.1172/JCI174508>.

Research In-Press Preview Pulmonology

Graphical abstract



Find the latest version:

<https://jci.me/174508/pdf>



Mechanosensitive channels TMEM63A and TMEM63B mediate lung inflation-induced surfactant secretion

Gui-Lan Chen^{1,*}, Jing-Yi Li^{1,*}, Xin Chen^{1,*}, Jia-Wei Liu^{1,*}, Qian Zhang^{1,*}, Jie-Yu Liu¹,
Jing Wen¹, Na Wang¹, Ming Lei¹, Jun-Peng Wei¹, Li Yi¹, Jia-Jia Li¹, Yu-Peng Ling¹,
He-Qiang Yi², Zhenying Hu³, Jingjing Duan³, Jin Zhang⁴, Bo Zeng^{1✉}

¹Key Laboratory of Medical Electrophysiology, Ministry of Education & Medical
Electrophysiological Key Laboratory of Sichuan Province, Institute of Cardiovascular
Research, Southwest Medical University, Luzhou, Sichuan, China.

²Department of Cardiothoracic Surgery, the Affiliated Traditional Chinese Medicine
Hospital of Southwest Medical University, Luzhou, Sichuan, China.

³Human Aging Research Institute and School of Life Sciences, Nanchang University,
Nanchang, Jiangxi, China.

⁴School of Basic Medical Sciences, Nanchang University, Nanchang, Jiangxi, China.

*These authors contributed equally to this work

✉Correspondence: Bo Zeng, Institute of Cardiovascular Research, Southwest Medical
University, Luzhou, Sichuan, 646000, China. Phone: 0086-830-3160619; E-mail:
zengbo@swmu.edu.cn.

ABSTRACT

Pulmonary surfactant is a lipoprotein complex lining the alveolar surface to decrease the surface tension and facilitate inspiration. Surfactant deficiency is often seen in premature infants and also children and adults with respiratory distress syndrome. Mechanical stretch of alveolar type 2 epithelial (AT2) cells during lung expansion is the primary physiological factor that stimulates surfactant secretion; however, it is unclear whether there is a mechanosensor dedicated for this process. Here we show that loss of mechanosensitive channels TMEM63A and TMEM63B resulted in atelectasis and respiratory failure in mice due to deficit of surfactant secretion. TMEM63A/B were predominantly localized at the limiting membrane of lamellar body, a lysosome-related organelle that stores pulmonary surfactant and ATP in AT2 cells. Activation of TMEM63A/B channels during cell stretch facilitated release of surfactant and ATP from lamellar bodies fused with the plasma membrane. The released ATP evoked Ca^{2+} signaling in AT2 cells and potentiated exocytic fusion of more lamellar bodies. Our study uncovered a vital physiological function of TMEM63 mechanosensitive channels, which makes the lung ready for the first breath at birth and maintains respiration through the life.

INTRODUCTION

Pulmonary surfactant is necessary for lowering surface tension of alveolar lining liquid and effective inspiration (1). Deficiency of pulmonary surfactant results in neonatal respiratory distress syndrome in premature infants (1), and is involved in a variety of pulmonary diseases in adults including acute respiratory distress syndrome, obstructive lung diseases, respiratory infections and pulmonary fibrosis (2). Inflation of the lung is known to stimulate pulmonary surfactant secretion via mechanosensitive ATP release and Ca^{2+} -dependent pathways in alveolar epithelial cells (AECs) (3, 4). AECs are consisted of large and thin alveolar type 1 (AT1) cells for gas exchange, and cuboidal alveolar type 2 (AT2) cells for synthesis and secretion of pulmonary surfactant. In AT2 cells, pulmonary surfactant and ATP are stored in lamellar bodies (LBs), a specialized lysosome-related organelle (5).

A commonly accepted mechanism of lung inflation-induced surfactant secretion is that stretch of AECs causes ATP release into the alveolar surface, and then these released ATP evoke Ca^{2+} signaling in AT2 cells which promotes fusion of LBs to the plasma membrane and surfactant exocytosis (3, 4). However, there are still several critical questions not yet addressed: (i) How mechanical stretch induces ATP release? Both AT1 and AT2 cells have been proposed to be the sources of ATP by in vitro studies (6, 7), and the pathway of ATP release has not been consistently illustrated. (ii) Why ATP treatment can potently stimulate LB fusion to the plasma membrane, but is much less efficient than cell stretch in facilitating surfactant release (8)? (iii) It is unclear that the stretch-induced Ca^{2+} signals are only a response of P2 purinergic receptors to extracellular ATP, or contain a component contributed by a Ca^{2+} -permeable mechanosensitive channel directly activated by cell stretch.

To address these questions, the most important issue is to understand how mechanical stretch is sensed and transduced in AECs. It remains to be determined whether there is a primary mechanosensor in AECs that initiates or controls release of ATP and surfactant. Among various cellular structures and proteins that are capable of sensing mechanical forces, mechanosensitive ion channels are most relevant to Ca^{2+} signaling and exocytosis. Currently, only four types of mammalian ion channels are

generally accepted as *bona fide* mechanically-activated channels, including Piezo1/2, two-pore domain K⁺ channels (K_{2P}, TREK/TRAAK), transmembrane channel-like TMC1/2 and transmembrane 63 (TMEM63) channels (9-11). Although Piezo1 has been found to regulate ATP release in an AT1 cell line (12), its functional expression in AECs is not detected in mouse lungs in vivo (13). K_{2P} channels are widely expressed but not directly related to Ca²⁺ signaling due to their repolarizing action (14). TMC1/2 form mechanotransduction channels in cochlear hair cells and their mutations cause only hearing loss (15). As a most recently identified mechanosensitive channel (11, 16, 17), TMEM63B plays a critical role in hair cell survival and is essential for hearing (18), but the physiological functions of TMEM63A/B/C in other systems are unclear.

To elucidate the mechanosensitive pathways underlying alveolar distention-induced surfactant secretion, we investigated mechanical ventilation-induced Ca²⁺ transients in intact lungs and stretch-activated membrane conductance in ACEs. We demonstrate that the mechanosensitive channels TMEM63A and TMEM63B are mechanosensors in AECs that mediate lung inflation-induced release of surfactant and ATP, and their essential roles in maintaining the respiratory function.

RESULTS

Lung inflation-induced ATP-mediated Ca²⁺ transients in alveolar cells

Using a Cre-dependent tdTomato-GCaMP6f-expressing mouse line (19), we examined Ca²⁺ signals in different alveolar cell types after mechanical ventilation in intact lungs ex vivo. GCaMP6f is a green fluorescent protein (GFP)-based Ca²⁺ indicator and tdTomato is a Ca²⁺-insensitive red fluorescent protein fused to GCaMP6f as a reference for expression and localization. In the lung, SPC-Cre, Tek-Cre and Cx3cr1-CreERT2 facilitate relatively specific expression of tdTomato-GCaMP6f in AT2, endothelial and myeloid (mostly macrophages) cells respectively, while Ager-CreERT2 is functional in most AT1 and ~10% AT2 cells (Figure 1A and Supplemental Figure 1). Post-inflation Ca²⁺ transients were observed in AT2, AT1 and endothelial cells, but not macrophages (Figure 1B and Supplemental Videos 1-5). The Ca²⁺ transients were most evident in AT2 cells, and relatively sparse in AT1 and endothelial

cells (Figure 1B); however, the duration of each Ca^{2+} transient was longer in endothelial cells than AT1 and AT2 cells (Figure 1C). The Ca^{2+} transients were significantly suppressed by suramin, a non-selective inhibitor of P2 purinergic receptors, and abolished by apyrase, an ATP diphosphohydrolase (Figure 1D), suggesting that they were triggered by ATP that released to alveolar surface upon mechanical ventilation. Additionally, the phospholipase C (PLC) inhibitor U-73122 also robustly reduced Ca^{2+} transients in AT2 cells (Figure 1D), confirming the involvement of P2Y receptors via the G_q -PLC- IP_3 receptor (IP_3R) pathway (20, 21). The consistent action of suramin, apyrase and U-73122 largely excluded the ATP-independent off-target effects of suramin and U-73122 (22, 23). However, genetic ablation of P2 receptors in AT2 cells, such as P2X4, P2X7, P2Y2 and P2Y6 (24), would provide more substantial evidence for their contribution to lung inflation-induced Ca^{2+} signals.

The density of AT2 cells showing Ca^{2+} transients (“spiking AT2”) increased with larger tidal volumes within physiological range (Figure 2A). Inflation for 5 min resulted in more Ca^{2+} transients in AT2 cells than 2-min inflation (Supplemental Figure 2A), and the percentage of spiking AT2 cells experienced exponential decay and diminished to basal level within 5 min after inflation (Figure 2B).

We then explored possible pathways of ATP release in the lungs. Gap junctional hemichannels, volume-regulated anion channel (VRAC) and Maxi Cl^- channel are proposed ATP-conducting channels widely expressed in many organs, including the lung (3). Blockers of gap junctions (Gap26 for Cx43, the dominant connexin isoform in the lung, and probenecid for pannexins) and Cl^- channels (DIDS and NPPB, non-selective for VRAC and Maxi Cl^-) did not significantly affect inflation-induced Ca^{2+} transients in AT2 cells (Figure 2C). The non-selective gap junctional blocker carbenoxolone (CBX) completely abolished the Ca^{2+} transients (Supplemental Figure 2B), however this turned out to be the consequence of its off-target inhibition on purinergic receptors, as evidenced by direct instillation of ATP into the lung (Supplemental Figure 2C) and Ca^{2+} response of A549 lung cancer cells to different concentrations of extracellular ATP (Supplemental Figure 2D).

To test LB-exocytic ATP release, we used clodronate, an inhibitor of vesicular

nucleotide transporter (VNUT) (25), to block ATP transport into LBs (5). Ex vivo lungs were mechanically ventilated for 2.5 h immediately after instillation of clodronate, and stopped for imaging Ca^{2+} in AT2 cells every 30 min. The density of spiking AT2 cells with clodronate showed a slow decrease similar as that of the Ctrl group within 1 h, which was followed by a dramatic decline that almost eliminated the Ca^{2+} spikes after 2 h (Figure 2D). This biphasic decline could be attributed to depletion of ATP-containing LBs by inflation-induced exocytosis after treatment with clodronate for 1 h. The remaining LBs may still be able to release surfactant, however the deficiency of exocytic ATP would no longer stimulate Ca^{2+} response in the cells. These results suggest that exocytosis of LBs is a probable pathway of mechanosensitive ATP release in AT2 cells.

Lastly, we used ultrafast imaging to detect Ca^{2+} signals in AT2 cells directly triggered by membrane stretch. However, we did not observe notable Ca^{2+} transients occurred immediately with the first pulse of mechanical ventilation (Supplemental Video 6). When the lung was pre-instilled with apyrase, only rarely occurred Ca^{2+} transients (presumably due to incomplete hydrolysis of extracellular ATP) were observed during a 5-min constant inflation with tidal volume of 500 μl (Supplemental Video 7). In line with this, either repetitive or constant stretch of the elastic substrate of primarily cultured AT2 cells failed to induce direct Ca^{2+} response in the presence of apyrase (Figure 2E; Supplemental Videos 8 and 9). In contrast, Ca^{2+} oscillations can be readily elicited by stretch in the absence of apyrase (Figure 2F; Supplemental Video 10). These results suggest a lack of highly Ca^{2+} -permeable mechanosensitive channel in AT2 cells.

Mechanosensitive currents in AT1 and AT2 cells

To investigate the mechanosensitive electrical activity of AECs, we first performed blunt-probe indentation on primarily cultured AT2 cells. Since the cells were loosely adhered to fibronectin-coated coverslip, most of them were pushed away once contacted with the probe and did not show convincing mechanosensitive currents before losing gigaseal. Considering that cell indentation is not a physiological way of

mechanical stimulation for cells in the lung, while membrane stretch is more relevant, we turned to use pressure clamp to examine the mechanosensitivity of AECs.

In pressure clamp under cell-attached mode, membrane stretch-induced macroscopic currents were observed for AT2 cells in culture and AT1 cells in acute lung slices, with similar properties including slow activation, no inactivation and pressure dependence (Figure 3A). Because in most recordings the currents increased exponentially with the pressure ranging from 0 to -140 mmHg and did not reach a plateau phase (Figure 3A, insets), the half-activation pressures (P_{50}) were not calculated. The amplitudes of currents were comparable between human and mouse AT2 cells, whereas a small subset of mouse AT1 cell recordings exhibited much larger currents (Figure 3B). For both human and mouse AT2 cells, cell-attached recordings with different cations in the pipettes showed that the mechanosensitive currents were mainly consisted of K^+ and Na^+ conductance, while Ca^{2+} , Mg^{2+} or $NMDG^+$ almost eliminated the inward currents (Supplemental Figure 3, A and B). The permeability of K^+ was slightly higher than Na^+ , and that for Ca^{2+} and Mg^{2+} were much lower (Figure 3C). The dramatically higher permeability of Na^+/K^+ over Ca^{2+} was confirmed by inside-out recordings (Supplemental Figure 3C). At negative membrane potentials of -27 to -63 mV in primary AT2 cells (26), the stretch-activated ion flow should be mainly Na^+ influx other than K^+ efflux.

We also detected single-channel activities in some recordings on AT2 cells, which are presumably epithelial Na^+ channel (ENaC) currents that have been widely recognized (27). However, these single-channel currents are insensitive to membrane stretch (Supplemental Figure 3D), and the above-mentioned stretch-activated macroscopic currents were not observed in these recordings, suggesting that these two types of channels do not coexist in the same membrane patches. To investigate the identity of ion channel that generates the stretch-activated currents, we used non-selective blockers for ENaC (amiloride), two-pore domain K^+ channels (quinine), gap junctional hemichannels (CBX) and Piezo channels (ruthenium red) in the pipette and bath solutions, however none of these agents exhibited significant effect (Figure 3D), indicating that the stretch-activated currents we observed are not generated by channels

sensitive to these blockers, including the four mentioned above. The currents were also insensitive to acidic extracellular pH (Figure 3D), suggesting that they were not conducted by proton channels, acid-sensitive cation channel (ASIC) or proton-activated Cl⁻ channel (PAC).

Due to the unusual large size of LBs (0.1-2.4 μ m) (28), they are very likely to be mechanically stressed during the stretch of AT2 cells. Therefore, we also examined the mechanosensitivity of endolysosomal (EL) system in AT2 cells, of which the overwhelming majority are LBs. The small molecule vacuolin-1 was used to induce fusion of LB/EL into giant vesicles large enough (>4 μ m) for patch clamp (29). The enlarged LB/EL vesicles in AT2 cells were isolated and pressure clamped under vesicle-attached configuration. The mechanosensitive currents of LB/EL vesicles were evident, with slow-activating and non-inactivating properties similar as the plasma membrane currents (Figure 3E). However, the current amplitudes of LB/EL vesicles measured at -60 mV/-60 mmHg are comparable with the plasma membrane currents at -80 mV/-80 mmHg (Figure 3, B and F), suggesting that LBs are more electrically sensitive to membrane stretch.

TMEM63A/B knockout results in atelectasis, pulmonary edema and respiratory failure

In search of the molecular identity of stretch-activated ion channel in AECs, we found that TMEM63B, a recently identified mechanosensitive channel (16, 17), is highly expressed in both AT1 and AT2 cells, according to single-cell RNA sequencing data from human and mouse lungs (Supplemental Figure 4). TMEM63A, a close homolog of TMEM63B, is also expressed in AT1 and AT2 cells at relatively lower levels (Supplemental Figure 4).

To explore the physiological function of TMEM63B, we generated constitutive *Tmem63b*-knockout (63b^{-/-}) mice and found most (~82%) of 63b^{-/-} mice died at birth without alveolar expansion (Figure 4, A and B, Supplemental Table 1 and Supplemental Figure 5). However, the remaining 63b^{-/-} neonates that were able to breathe all survived as their wildtype (wt) and 63b^{+/-} littermates (Figure 4A), with normal lung structure and

function (Supplemental Figure 5). Considering the co-expression of TMEM63A and TMEM63B in most tissues, we suspected that TMEM63A would complement the function of TMEM63B when it was absent. Constitutive *Tmem63a*-knockout ($63a^{-/-}$) mice were all viable from neonatal to late adult stages (Figure 4A and Supplemental Table 1). Combined deletion of *Tmem63a* and *Tmem63b* resulted in death of all $63a^{-/-} 63b^{-/-}$ neonates with phenotype same as $63b^{-/-}$ mice died at birth (Figure 4A, Supplemental Table 1 and Supplemental Figure 5).

To validate the roles of TMEM63A and TMEM63B in AECs, we generated *Tmem63a* and *Tmem63b* conditional double knockout (*Tmem63a/b* cDKO) mice with gene deletions in AT1 and AT2 cells using Aqp5-Cre and SPC-Cre, respectively. Deficiency of *Tmem63a/b* in AT1 and ~50% AT2 cells ($Aqp5-Cre^{+/-} 63a^{fl/fl} 63b^{fl/fl}$ ($Aqp5-63ab$), Supplemental Figure 1) did not affect the viability of mice at all developmental stages (Figure 4C, Supplemental Table 1 and Supplemental Figure 5). In contrast, only ~20% $SPC-Cre^{+/-} 63a^{fl/fl} 63b^{fl/fl}$ mice ($SPC-63ab$, with Cre activity in all AT2 cells) survived at the day of birth (P0), but all died before P7 due to respiratory failure (Figure 4C, Supplemental Table 1 and Supplemental Figure 5). We also generated $Lyz2-Cre^{+/-} 63a^{fl/fl} 63b^{fl/fl}$ ($Lyz2-63ab$) mice using *Lyz2-Cre* that expressed in macrophages and ~6% AT2 (Supplemental Figure 1); however no respiratory phenotype was observed for these mice (Supplemental Table 1 and Supplemental Figure 5).

To investigate the function of TMEM63A and TMEM63B in alveolar epithelium at adult stage, we bred *Tmem63a/b* cDKO mice with tamoxifen-inducible gene deletions in AT1 and AT2 cells using Ager-CreERT2 ($Ager-63ab$) and Sftpc-CreERT2 ($Sftpc-63ab$), respectively. To achieve *Tmem63a/b* cDKO in both AT1 and AT2 cells, we generated double-Cre $Ager-CreERT2^{+/-} Sftpc-CreERT2^{+/-} 63a^{fl/fl} 63b^{fl/fl}$ ($Ager-Sftpc-63ab$) mice, and $Nkx2.1-CreERT2^{+/-} 63a^{fl/fl} 63b^{fl/fl}$ ($Nkx2.1-63ab$) mice with Cre activity in AT1 and ~80% AT2 cells (Supplemental Figure 1). $Ager-63ab$ mice did not show any abnormal phenotype after tamoxifen induction for 5 consecutive days (Figure 4D, Supplemental Table 1 and Supplemental Figure 5). $Sftpc-63ab$ mice exhibited signs of atelectasis and progressed into respiratory failure from the 10th day after the last tamoxifen injection and all animals died no later than the 14th day (Figure 4, D-G and

Supplemental Table 1). Lung lobes in *Sftpc*-63ab mice collapsed gradually and could not be inflated by mechanical ventilation (Supplemental Video 11). *Ager*-*Sftpc*-63ab mice had an earlier onset of atelectasis and respiratory failure, with a maximal surviving period of 12 days after tamoxifen induction (Figure 4, D-G and Supplemental Table 1). However, *Nkx2.1*-63ab mice retained normal lung function and survived as their *63a^{fl/fl}63b^{fl/fl}* (*Ctrl*-63ab) littermates (Figure 4D, Supplemental Table 1 and Supplemental Figure 5). These results suggest that only complete ablation of *Tmem63a* and *Tmem63b* in all AT2 cells (*Sftpc*-63ab) could result in lethal respiratory phenotype in mice. In *Aqp5*-63ab and *Nkx2.1*-63ab mice, the *Cre⁻* AT2 cells with intact *Tmem63a* and *Tmem63b* could compensate for the loss of the two genes in *Cre⁺* AT2 cells. Surfactant secreted from these *Cre⁻* AT2 cells is sufficient to facilitate effective lung inflation during breathing.

All atelectasis-affected mice experienced dramatic decline of saturation of peripheral oxygen (*SpO₂*) started from 24 h before death (Figure 4H). The lung weights were much higher in *Sftpc*-63ab and *Ager*-*Sftpc*-63ab mice than *Ctrl*-63ab littermates due to pulmonary edema (Figure 4I). Dysfunction of the lung ultimately resulted in dramatic loss of body weight (Figure 4J). The concentrations of secreted SPC, dipalmitoylphosphatidylcholine (DPPC, the major surfactant lipid) and ATP in bronchoalveolar lavage fluid collected at the 10th day after tamoxifen induction were significantly lower in *Sftpc*-63ab and *Ager*-*Sftpc*-63ab mice than *Ctrl*-63ab littermates (Figure 4K and Supplemental Figure 6). These *in vivo* data indicate that *TMEM63A* and *TMEM63B* in AT2 cells are essential for surfactant secretion, and their activity in AT1 cells can further support normal lung function.

To examine whether *Tmem63a/b* cDKO has caused the respiratory phenotype by compromising AT2 cell survival and LB biogenesis, we stained AT2 cells with three markers, LysoTracker and Pro-SPB/Pro-SPC, in acute lung slices and paraffin sections, respectively. The three markers all showed that the density of AT2 cells in the lungs was not affected by *Tmem63a/b* cDKO (Supplemental Figure 7), although some differences were observed for the staining intensity of LysoTracker and Pro-SPC. There were more AT2 cells with large and bright LysoTracker spots (LBs) in cDKO mice

(Supplemental Figure 7A). The expression of Pro-SPB was comparable between Ctrl and cDKO mice (Supplemental Figure 7B). Staining intensity of Pro-SPC was significantly reduced in cDKO mice (Supplemental Figure 7C), which we found was actually caused by knock-in of CreERT2 in the endogenous *Sftpc* locus, as the *Sftpc*-CreERT2 mice showed similar level of Pro-SPC reduction (Supplemental Figure 7D). Due to reduced expression of Pro-SPC, the level of secreted mature SPC was also lower in *Sftpc*-CreERT2 mice (this impairment was much weaker than that caused by *Tmem63a/b* cDKO), however secretion of surfactant lipids was not affected (Supplemental Figure 7E). These results suggest that *Tmem63a/b* cDKO does not change the identity and viability of AT2 cells, but caused enlargement and malfunction of LBs.

TMEM63A/B are required for lung inflation-induced Ca^{2+} transients and surfactant release

To investigate lung inflation-induced Ca^{2+} transients in AT2 cells deficient for TMEM63A and TMEM63B, we delivered adeno-associated viruses (AAV) carrying Cre-dependent jGCaMP7s-mCherry into *Sftpc*-63ab mouse lungs via intratracheal instillation. jGCaMP7s is an optimized version of GFP-based Ca^{2+} indicator (30) and mCherry is a red fluorescent protein serving as Ca^{2+} -insensitive reference. The *Sftpc*-CreERT2 mice were used as control and instilled with AAV in the same way. As indicated by the density of mCherry⁺ cells, the transduction efficiency was comparable between *Sftpc*-63ab and *Sftpc*-CreERT2 mice (Figure 5, A and B). However, in contrast to the evident inflation-induced Ca^{2+} transients in *Sftpc*-CreERT2 mouse lungs, no Ca^{2+} transients were observed in *Sftpc*-63ab lungs, either in lobes still inflatable or fully collapsed (Figure 5C and Supplemental Videos 12-14).

The absence of inflation-induced Ca^{2+} transients in AT2 cells would result from deficiency of mechanosensitive ATP release, hence we hypothesized that supply of exogenous ATP to alveoli would rescue the lethal phenotype of *Tmem63a/b* cDKO. Unfortunately, daily inhalation of aerosolized ATP solution after tamoxifen induction did not significantly extend the surviving period of *Sftpc*-63ab and Ager-*Sftpc*-63ab

mice (Figure 5D). Primary AT2 cells from Sftpc-63ab mice were able to respond to extracellularly applied ATP with Ca^{2+} transients (Figure 5E) and LB fusion to the plasma membrane, as indicated by staining of concentrated surfactant phospholipids with the FM4-64 dye that entered LBs through the fusion pore (Figure 5F). When ATP-treated AT2 cells from Ctrl-63ab mice were subject to cyclic strain, some of the fused LBs lost FM4-64 fluorescence within 10 min (Figure 5F, upper panels), suggesting release of phospholipid content. However, such phenomenon was not observed in Sftpc-63ab AT2 cells treated in the same way (Figure 5F, lower panels). After cyclic strain for 2 h, Ctrl-63ab cells lost most of the FM4-64⁺ pre-fused LBs, suggesting very high exocytic activity induced by cell stretch (Figure 5G). In contrast, the number of FM4-64⁺ LBs in Sftpc-63ab cells was only slightly reduced (Figure 5G), which indicates that surfactant from pre-fused LBs cannot be efficiently released without TMEM63A/B even in the presence of ATP and mechanical stretch. In AT2 cells without ATP treatment, cyclic strain for 2 h significantly increased the number of FM4-64⁺ LBs in Ctrl-63ab cells, but had no effect on Sftpc-63ab cells (Figure 5H). A schematic description for these results is provided in Supplemental Figure 8.

When ATP was washed out and the cells were maintained at static condition, some fused LBs became lumenally reacidified in 20 min (indicated by appearance of LysoTracker fluorescence overlapped with FM4-64 staining; Figure 5I), suggesting that the fusion pore can be closed if the exocytosis of fused LBs failed. Transmission electron microscopy showed more enlarged LBs with disordered internal membrane sheets in Sftpc-63ab AT2 cells than control cells (Figure 5, J and K), which is consistent with the observation from LysoTracker staining in live AT2 cells in acute lung slices (Supplemental Figure 7A), and likely caused by abnormal contact and fusion between LBs that cannot be exocytosed in the absence of TMEM63A/B.

TMEM63A/B are essential for the mechanosensing in AECs

To further explore the role of TMEM63A/B in the mechanotransduction in AECs, we examined the mechanosensitive currents in AT1/AT2 cells and LB/EL vesicles from *Tmem63a/b* cDKO mice. Pressure clamp under cell-attached mode detected only

negligible stretch-activated currents in AT1 and AT2 cells from cDKO mice, while the mechanosensitive currents were totally abolished in the LB/EL vesicles from TMEM63A/B-deficient AT2 cells (Figure 6A).

Due to the lack of reliable antibodies against endogenous TMEM63A and TMEM63B, we were unable to directly detect their localization in AT1 and AT2 cells with immunofluorescence. Instead we performed genome editing in mouse lungs with CRISPR/Cas9 technology to knock-in 2×V5-tag sequence immediately after the start codon of *Tmem63b* gene. Immunofluorescence against V5 tag showed that TMEM63B was mainly localized at the limiting membrane of LBs in AT2 cells, as indicated by the marker LAMP1 (Figure 6B). No obvious immunofluorescence was detected at the plasma membrane of AT1 and AT2 cells, probably because the density of TMEM63B proteins at cell surface is much lower than LBs. Fusion of LBs with the plasma membrane may allow diffusion of small amount of TMEM63B from LBs to cell surface.

Overexpression of fluorescent protein-tagged TMEM63A/B in Hela cells and subsequent treatment with vacuolin-1 revealed that both TMEM63A/B were present at endolysosomal membranes but not completely overlapped, while TMEM63B was additionally localized at the plasma membrane (Supplemental Figure 9). Co-transfection with the early endosome marker RAB5A, and staining with LysoTracker Green, the indicator of acidic lysosome and late endosome, suggest the preference of TMEM63B for early endosome and universal presence of TMEM63A in early/late endosomes and lysosomes (Supplemental Figure 10). The presence of TMEM63B at the plasma membrane was further confirmed by non-permeabilized immunofluorescence against V5 tag fused at the N terminus of TMEM63B (V5-TMEM63B), which is extracellularly located (Supplemental Figure 11A). The same strategy produced very dim staining against Myc-TMEM63A, suggesting that TMEM63A is rarely trafficked to the plasma membrane (Supplemental Figure 11A).

Large stretch-activated currents were recorded from 7 out of 20 Hela cells transfected with TMEM63B (Figure 6C), and exhibited the same properties as the currents in AECs, including slow activation, no inactivation and higher permeability for Na^+/K^+ than Ca^{2+} (Figure 6, D-F). This suggests that TMEM63B could recapitulate

the properties of the mechanosensitive channel in AECs. Although Ca²⁺ permeability of TMEM63B has been proposed by a previous study based on hypotonic stimulation (18), we suppose this would be questionable due to some technical issues we reviewed recently (31), and more importantly, we did not record convincing hypotonicity-induced currents in TMEM63B-transfected LRRC8A-KO HEK293 cells without VRAC activity (Supplemental Figure 3E).

As to the low ratio of successful recordings for large stretch-activated currents in Hela cells, we found that TMEM63B was not evenly distributed but formed clusters at the plasma membrane, with mean density of ~1 cluster/ μm^2 (Supplemental Figure 11B). The area of the micropipette tip in our experiment was ~1 μm^2 , which can only accommodate one TMEM63B cluster in average, so negative recordings cannot be avoided.

Consistent with previous report on TMEM63-transfected HEK293 cells (17), whole-cell recordings in TMEM63B-transfected Hela cells did not show any cell indentation-induced currents. In TMEM63A/B-transfected Hela cells, the vacuolin-1-induced vesicles were too small to perform patch clamp recordings (Supplemental Figure 9). This implies that TMEM63A/B may function in Hela cells to prevent the fusion of endolysosomes, however their ion channel activity cannot be directly assessed due to technical limitation.

Human TMEM63A/B rescued the lethal phenotype of *Tmem63a/b* cDKO mice

We delivered AAVs encoding human TMEM63A (h63A) and TMEM63B (h63B) into the lungs of Ager-Sftpc-63ab mice by intratracheal instillation at the first day of tamoxifen injection. Both h63A and h63B successfully rescued the mice from respiratory failure, with 5 out of 6 mice receiving h63A and 4 of 5 mice receiving h63B survived for two months after tamoxifen induction (Figure 7A), before they were sacrificed for sampling. The lungs from these mice showed normal morphology and structure, without signs of atelectasis or edema (Figure 7B). In contrast, a mechano-insensitive pore mutant of h63B (Y572A, Supplemental Figure 12) failed to compensate for the loss of endogenous TMEM63A/B in cDKO mice (Figure 7, A and

B). The transduction efficiency of h63A, h63B and h63B-Y572A AAVs were comparable, all with high expression in AT2 cells and prominent localization at the limiting membrane of LBs (Figure 7C). These results demonstrate that the mechanosensitive channel activity of TMEM63A/B is crucial for normal lung function, and this role of TMEM63A/B is conserved between mouse and human.

DISCUSSION

In the present study, we demonstrate that TMEM63A and TMEM63B channels essentially support alveolar expansion and breathing in both neonatal and adult mice by enabling sufficient surfactant secretion. Although the mechanism that triggers the first breath at birth is complicated (32, 33), pulmonary surfactant plays an essential role in this process by reducing the surface tension of the alveolar lining liquid, i.e. the resistance to breathing in the air. Preterm infants often develop neonatal respiratory distress syndrome due to surfactant deficiency (1). Little is known about the regulation of surfactant secretion in developing lung at prenatal stage. Mechanical force generated from inhalation of small amount of amniotic fluid by fetal breathing movements before birth is essential for differentiation of AT1 cells in lung development (34), which we suppose would also stimulate surfactant secretion in the fetal lung. Stretch-activated currents were detected in AT2 cells from E17.5 fetal mice (Supplemental Figure 3F), with the same properties as TMEM63 currents in adult AT2 cells. Therefore, the deficiency of TMEM63A/B channels may diminish alveolar surfactant levels and cause the failure of breath after birth, via the same mechanism we illustrate in adult lungs.

Surfactant dysfunction is a characteristic of acute respiratory distress syndrome (ARDS) in adult patients (35). Surfactant activity is compromised in ARDS due to a series of pathological changes, such as inflammatory damage of AT2 cells, reduced surfactant synthesis and secretion, altered surfactant composition, accelerated surfactant breakdown, and functional inhibition by plasma components (36). As a consequence, alveolar surface tension is increased, which leads to poor alveolar compliance, alveolar collapse and severe hypoxemia. Despite these findings, exogenous surfactant therapy only improved oxygenation in some ARDS patients, but

428 did not produce survival benefit (37, 38). This is generally attributed to the
429 heterogeneity of ARDS and lack of an optimal strategy of therapy, including
430 compositions and doses of surfactant, and the time and methods of surfactant delivery
431 (36, 39). Further studies on the pathophysiological mechanisms of ARDS and surfactant
432 dysfunction are required to improve the efficacy of surfactant therapy. It will be
433 interesting to investigate whether the expression and activity of TMEM63A/B channels
434 are impaired in ARDS, and determine their potential to be therapeutic targets.

435 It should be noted that although we have found that the concentrations of SPC and
436 DPPC, two main components of pulmonary surfactant, were dramatically reduced in
437 the bronchoalveolar lavage fluid (BALF) of *Tmem63a/b* cDKO mice, surface tension
438 of the BALF needs to be measured directly using a pulsating bubble surfactometer or
439 Wilhelmy balance (40) to provide definitive evidence for surfactant deficiency, which
440 is a limitation of our study.

441 The mechanisms of mechanosensitive ATP release have been extensively studied
442 in various cell types, with three possible pathways suggested: ATP-conducting channels,
443 vesicular exocytosis and membrane leakage (3). Channels proposed to permeate ATP
444 include gap junctional hemichannels (connexins and pannexins), calcium homeostasis
445 modulator 1 (CALHM1), VRAC and Maxi Cl⁻ channels (41). Connexins, pannexins
446 and CALHM1 are large-pore channels nonselective for cations, anions and small
447 molecules (42). If these channels are opened by membrane stretch to allow ATP
448 permeation, they should also permeate small ions such as Ca²⁺, Na⁺, K⁺ and Cl⁻. As we
449 did not observe stretch-activated Ca²⁺ influx into AT1 and AT2 cells, these channels are
450 unlikely to conduct mechanosensitive ATP release from AECs. In agreement with this,
451 blockers of connexins and pannexins did not inhibit lung inflation-induced ATP-
452 mediated Ca²⁺ transients in AT2 cells. As to CALHM1, its expression is not detected in
453 AT1 and AT2 cells by single-cell RNA sequencing (Mouse Cell Atlas and Human
454 Protein Atlas). Similar as these non-selective channels, ATP leakage due to stretch-
455 induced membrane injury should also be accompanied by immediate and massive Ca²⁺
456 influx (3), which was not observed in our experiment.

457 VRAC and Maxi Cl⁻ are recognized as anion-selective channels and thus they may

conduct negatively charged ATP with no or very weak cation permeation (43). Nevertheless, we found that blockers of these channels did not affect lung inflation-induced ATP-mediated Ca^{2+} transients in AT2 cells. Moreover, patch-clamp recordings indicate that the stretch-activated channel in AT2 cells is highly permeable to K^+ and Na^+ and the single-channel conductance is too small to resolve, which are apparently not the properties of VRAC and Maxi Cl^- channel. Therefore, these two types of anion channels are unlikely to play an important role in mechanosensitive ATP release from AT2 cells.

By blocking ATP transport into LBs with clodronate, we demonstrate that exocytosis from LBs is probably the major pathway of lung inflation-induced ATP secretion, which is consistent with previous findings that ATP is enriched in LBs (5) and released independently of ATP-conducting channels (7). It needs to be mentioned that the membrane permeability of clodronate is very low and it is normally packed into liposomes for intracellular delivery (44). However, as a bisphosphonate, clodronate may be transported into AT2 cells by the sodium-phosphate cotransporter SLC34A2, which is abundantly expressed in AT2 cells (45). In addition, bisphosphonate can be endocytosed into endolysosomes and then released into cytosol via the SLC37A3-ATRAID transporter complex in osteoclasts (46). The same pathway may also exist in AT2 cells since SLC37A3 and ATRAID are ubiquitously expressed.

Previous studies have described the effects of ATP, Ca^{2+} and cell stretch on surfactant secretion (4), however some mechanistic steps are still unclear. Stimulation with ATP efficiently promotes LB fusion to the plasma membrane, but its effect on subsequent surfactant release is limited and can be substantially enhanced by cell stretch (8). In line with this, the expansion of fusion pore has been demonstrated to be a slow and discontinuous process at static condition (47). This raised the question how cell stretch promotes surfactant release from fused LBs.

Unlike other exocytic materials such as neurotransmitters, pulmonary surfactant is a bulky and hydrophobic lipoprotein complex that cannot be released into extracellular fluid simply by diffusion through the fusion pore (48). After LB fusion to the plasma membrane, surfactant is still trapped in LBs and spontaneous expansion of the fusion

pore occurs slowly (47). The constrictive fusion pore therefore acts as a mechanical barrier obstructing surfactant release (8). Moreover, even the fusion pore is dilated, surfactant does not readily diffuse out of fused LBs (48). A mechanical force that compresses LBs is required to squeeze the surfactant out in an “all-or-none” manner (8). It has been found that the formation and contraction of actin coats on fused LBs are essential for surfactant secretion (48, 49). Contraction of actin coats was visualized with GFP-tagged actin overexpressed in ATP-treated AT2 cells at static condition (48), which is the only observation for the shrinking process of fused LBs so far. However, it is unclear that the contraction of actin coats is an active process that applies force on LBs, or a passive reassembling process associated with shrinking of LBs to prevent backward enlargement, as the ATP-activated cation channel P2X4 at the limiting membrane of LBs also plays a role in fusion pore expansion and surfactant release (5, 50).

Based on our findings that TMEM63A/B-deficient AT2 cells failed to release surfactant in response to cell stretch, we propose a TMEM63A/B-mediated mechanism for this process (Graphical abstract): When AT2 cells are stretched during inspiration, LBs are also mechanically stressed due to their large size and association with cytoskeleton (51). Then TMEM63A/B at the limiting membrane of LBs are activated due to increased membrane tension. For LBs fused on the plasma membrane, stretch-activated Na^+ flux from LB lumen to cytosol through TMEM63A/B can theoretically generate an osmotic force that shrinks fused LBs and squeezes surfactant out to the cell surface, as the mode demonstrated in neuroendocrine cells (52). Additionally, as TMEM63A/B activity is also detected at the plasma membrane, the osmotic gradient can potentially cause water influx and transient cell swelling, which may help to expand the fusion pore. Because ATP is co-released with surfactant from fused LBs (5), this hypothesis also explains how mechanosensitive ATP release is conducted. Unfortunately, since it is currently a technical challenge to visualize the size of LBs and surfactant release during cell stretch, which requires very high resolution, wide field of view (due to cell movement), perfect focus and ultrafast imaging, we are unable to obtain direct evidence for the shrinkage of fused LBs during cell stretch.

For LBs, the stretch-activated currents measured at -60 mmHg and -60 mV were similar as (mouse) or even larger (human) than that of the plasma membrane at -80 mmHg and -80 mV (Figure 3, B and F), suggesting that it is more sensitive to membrane stretch, which further supports our hypothesis of osmotic force-driven exocytosis of LBs. As for LBs not fused with the plasma membrane (with intact limiting membrane), activation of TMEM63A/B may also cause osmotic shrinkage, but the size of LBs can be quickly recovered by counteracting ion flux via other channels and transporters after stretch, without loss of luminal contents.

In patch clamp experiment, we found that cell indentation is not a proper way to activate TMEM63A/B, and very high vacuum pressure is required to induce robust stretch-activated current in cell-attached recording. It needs to be explained that the vacuum pressure used in pressure clamp cannot be directly compared with the air pressure that drives alveolar expansion. We calculated negative pressure-induced membrane area changes in micropipette under cell-attached configuration using published data (53). Compared to the membrane area at 0 mmHg, -100 mmHg pressure only increased the area by ~85% (Supplemental Figure 13). In contrast, the surface area of AECs can expand for several folds during breathing (54, 55), with transpulmonary pressure (alveolar pressure minus intrapleural pressure) less than 10 mmHg as the driving force (56). Therefore, although very high pressure is used in our experiment, the extent of membrane stretch is still within the physiological range. Lateral stretch of AECs in vivo should be much more efficient in increasing membrane tension and activating mechanosensitive channels.

In lung mechanobiology, Piezo2 channel has been recognized as the stretch sensor in sensory neurons innervating the airway, which limits over-inflation of the lung by triggering the Hering-Breuer inspiratory reflex (57). It will be interesting to investigate whether lung inflation-induced TMEM63 channel activity contributes to mechanotransduction in sensory neurons, either through ATP signaling or direct activation in neurons. As genetic variants of *TMEM63A/B/C* have been identified in patients with neurodevelopmental disorders (58-60), further studies are required to understand the functions of TMEM63 channels in the nervous system. In human,

TMEM63A is highly expressed in oligodendrocytes, and *TMEM63B/C* are present in both neurons and glial cells (31). Similarly, *Tmem63a* is absent, while *Tmem63b/c* are detected in most mechanosensory neurons in mouse dorsal root ganglion (61). The function of TMEM63 channels is critically dependent on their subcellular localization, which is completely unknown in neurons and glial cells at the moment. Considering the broad expression of TMEM63A/B (31), investigations on their roles in other mechanically active organs, such as the heart, gut and bladder, are also expected.

In summary, we found that TMEM63A/B mechanosensitive channels in AT2 cells control the release of pulmonary surfactant and ATP by sensing and transducing mechanical force on LBs during alveolar expansion. Deficiency of TMEM63A/B results in surfactant insufficiency in alveoli, which subsequently causes atelectasis and respiratory failure. The exact mechanism of TMEM63A/B in promoting surfactant release from LBs and their role in AT1 cells need to be further investigated.

MATERIALS AND METHODS

Mice

Knockout or transgenic mouse strains were purchased from qualified providers listed in Supplemental Table 2. To obtain constitutive *Tmem63a/b* double knockout mice, *Tmem63a*^{-/-}*Tmem63b*^{+/-} mice were first generated by crossing *Tmem63a*^{+/-} and *Tmem63b*^{+/-} mice for 2 generations and then used to breed *Tmem63a*^{-/-}*Tmem63b*^{-/-} mice. For *Tmem63a/b* cDKO, *Tmem63a*^{fl/fl}*Tmem63b*^{fl/fl} mice were first generated and then crossed with Cre mice for 2-3 generations to obtain Cre⁺*Tmem63a*^{fl/fl}*Tmem63b*^{fl/fl} mice. The mice were maintained in the Experimental Animal Center of Southwest Medical University in specific pathogen free (SPF) conditions with standard 12-h light and dark cycles and free access to food and water. Mice of both sexes at different ages were used in the experiment.

Cell line

Hela cells were purchased from American Type Culture Collection (ATCC) and cultured in DMEM/F-12 medium with 10% fetal bovine serum (FBS), 100 units/ml penicillin and 100 µg/ml streptomycin in a 5% CO₂ incubator at 37°C (abbreviated as “normal culture condition” hereafter). The cells were tested negative for mycoplasma contamination, transfected with plasmids using Lipofectamine 2000 (2 µl/µg DNA) and plated on glass coverslips for fluorescent imaging or patch clamp experiment.

Ca²⁺ imaging in ex vivo lungs

GCaMP-expressing mice were sacrificed with CO₂ inhalation and subject to endotracheal intubation with a blunted syringe needle (tracheal catheter). The lung, heart and intact trachea were carefully dissected together from the mice. The trachea was tightly tied on the tracheal catheter with surgical sutures during dissection. The lung was placed on a glass coverslip on the microscope and the tracheal catheter was connected to a ventilator. The frequency of ventilation was 1 Hz in all experiment. The GCaMP, tdTomato and mCherry fluorescence were excited and captured with FITC, TRITC and Texas red filter sets, respectively. Focus was adjusted before and after

mechanical ventilation for best-quality imaging. Nikon Eclipse Ti inverted microscope, ORCA-Flash4.0 sCMOS camera (Hamamatsu, Japan) and NIS-Elements software (Nikon, Japan) were used for fluorescent imaging.

For chemical blockers used the lungs, we used 2-3 folds higher concentrations than that normally used for cultured cells, since the compounds could be diluted by alveolar fluid during mechanical ventilation. Chemicals were diluted in 100 μ l physiological extracellular solution (in mM: 140 NaCl, 5 KCl, 1 MgCl₂, 2 CaCl₂, 10 HEPES and 10 glucose, pH7.4) and instilled into the lung via the tracheal catheter.

Isolation and culture of AT2 cells

After euthanasia with CO₂, the lung and heart of mice were surgically exposed. Sterile 0.9% NaCl was perfused from right heart apex until the heart was visually bleached. Then endotracheal intubation was performed and 2 ml dispase solution (1 mg/ml dissolved in PBS, Sigma) was slowly infused into the lung, and left for 5 min. Immediately after injection of 0.5 ml low melting point agarose (1%, dissolved in PBS), cover the lung with ice to solidify the agarose in 2 min. The lung was removed from mouse and digested in dispase solution for 45 min at room temperature on a shaker, and then transferred to 7 ml 0.01% DNase I (dissolved in DMEM/F-12) and cut into small pieces using fine scissors. Cell suspension was collected for filtration with a 100- μ m cell strainer and centrifuged at 900 rpm for 4 min at 4°C, and cultured in normal petri dish under normal culture condition. After 12 h, collect unattached cells (mainly AT2 cells) by centrifuging at 900 rpm for 4 min at 4°C, and plate the cells on glass coverslips or silicon membranes (0.1-mm thickness) precoated with fibronectin (50 μ g/ml overnight) under normal culture condition.

Human AT2 cells were isolated from lung tissues according a published protocol (62) with minor modifications. Briefly, the samples were instilled with PBS to remove blood and digested with 0.25% trypsin for 45 min at 37°C. The tissue was then cut into fine pieces in the presence of FBS, and treated with DNase I. The cells were filtered with 100 μ m cell strainer and the following steps were proceeded as mouse AT2 cells above.

Preparation of lung slices

Endotracheal intubation was performed on euthanatized mice. Infuse 2 ml 1.5% low melting point agarose solution (in mM: 58.2 NaCl, 2.7 KCl, 0.9 CaCl₂, 0.4 MgSO₄, 0.6 NaH₂PO₄, 12.6 HEPES, 13 NaHCO₃, and 8.4 glucose, pH7.2) into the lung, and cover the lung with crushed ice for 20 minutes. Then the lung was removed from the mouse and cut into slices of 250 µm thickness in 4°C cold slicing solution (in mM: 116.4 NaCl, 5.4 KCl, 1.8 CaCl₂, 0.8 MgSO₄, 1.2 NaH₂PO₄, 25.2 HEPES, 26.1 NaHCO₃, and 16.7 glucose, pH7.2) using a vibratome (Leica VT 1000S). The lung slices were stored in slicing medium at 4°C for fluorescent imaging or electrophysiological experiments.

Electrophysiology

Mouse and human AT2 cells were characterized from crude isolated cells by LysoTracker staining on LBs, which are much larger and brighter than lysosomes in other cell types. All recordings were performed at room temperature (~25°C).

Macroscopic stretch-activated currents of AT2 and transfected cells were recorded under cell-attached or inside-out configuration. Resistances of the micropipettes were 3-4 MΩ. Membrane patches were stretched by 500-ms negative pressure pulses through the glass micropipette. The negative pressures were generated by the High Speed Pressure Control device (HSPC-2, ALA-scientific) with -20 mmHg increase for each sweep and inter-sweep duration of 10 s. Signals were sampled at 10 kHz and filtered at 3 kHz.

For AT1 cells with *Tmem63a/b* cDKO (Ager-63ab), AAV carrying CMV-DIO-EGFP was instilled into the lung to label Cre⁺ cells with *Tmem63a/b* ablated. AT1-attached pressure clamp was conducted in acute lung slices in physiological extracellular solution. Resistances of the micropipettes were 3-4 MΩ. Only EGFP⁺ AT1 cells were considered authentic *Tmem63a/b* cDKO cells because Ager-CreERT2 does not induce DNA recombination in all AT1 cells.

To record mechanosensitive currents in LB/EL vesicles, AT2 cells were treated with 2.5 µM vacuolin-1 in culture medium overnight. Enlarged LB/EL vesicles were isolated and patch clamped under vesicle-attached configuration. Both the pipette and bath

solutions for LB/EL vesicles were physiological intracellular solution (in mM: 135 KCl, 10 NaCl, 0.5 MgCl₂, 3.8 CaCl₂, 10 HEPES and 10 EGTA, pH7.2). Resistances of the micropipettes were 5-7 MΩ. Pressure clamp with -10 mmHg increase for each sweep and inter-sweep duration of 10 s was conducted.

For ion selectivity assay, solutions including (in mM) 150 NaCl + 10 HEPES, 150 KCl + 10 HEPES, 100 CaCl₂ + 10 HEPES, 100 MgCl₂ + 10 HEPES and 150 NMDG-Cl + 10 HEPES (pH7.4 for all) were used for pressure clamp under cell-attached or inside-out configuration. Voltage steps from -100 to +100 mV or -80 to +80 mV with 20 mV increase and -80 mmHg pressure were applied. Liquid junction potentials were calculated in Clampex and corrected after experiments. Relative permeability to Na⁺ was calculated with the Goldman-Hodgkin-Katz Equation detailed in the reference (63).

Tamoxifen administration

Tamoxifen was dissolved in corn oil to 20 mg/ml by sonification and kept in dark. Both the CreERT2-positive and control mice were intraperitoneally injected with tamoxifen solution (75 mg/kg body weight per day) for 5 consecutive days.

Micro-computed tomography (microCT)

MicroCT for isoflurane-anesthetized mice was performed using the Siemens Inveon Multi-Modality System (Siemens Healthineers), with the following sampling parameters: 80 kV voltage, 500 μA current, 200 ms exposure, 220° rotation, 120 projections and 8.8 × 13.29 cm field of view. Acquisitions were reconstructed with Feldkamp's algorithm using software provided with the system. Computed intensities from representative areas of ~40 mm³ volume in left and right lungs were averaged as mean lung volume intensity.

Saturation of peripheral oxygen (SpO₂) monitoring

Mice were anesthetized with isoflurane and the hair of bilateral neck was removed with depilatory. A small collar clip with pulse oximeter sensor (MouseOx Plus, Starr Life Sciences) was placed on the neck to monitor the SpO₂. Data were recorded after the

mice were returned to their home cages and completely recovered from anesthetization.

Bronchoalveolar lavage

Immediately after euthanasia, mouse trachea was exposed and intubated. Gently infuse 1 ml PBS into the lung through the catheter and then aspirate it with a syringe. Repeat this procedure for 5 times and collect the bronchoalveolar lavage fluid (0.7-0.9 ml) into a tube placed on ice. After centrifugation at 400×g for 5 min at 4°C, the supernatant was immediately used or stored at -80 °C.

Immunofluorescence and hematoxylin & eosin (HE) staining

Lung tissues were fixed with 4% paraformaldehyde, dehydrated in 20-30% sucrose, frozen or paraffin embedded, and sectioned. Immunofluorescence on frozen/paraffin sections, and HE staining on paraffin sections were performed with general protocols (64). Information of antibodies is provided in Supplemental Table 2.

For cell surface immunofluorescence, Hela cells transfected with Myc-TMEM63A and V5-TMEM63B plasmids were washed 3 times with PBS, incubated with rat anti-Myc tag and rabbit anti-V5 tag primary antibodies diluted (1:500) with cold culture medium at 4 °C for 0.5 h, and then washed 3 times with cold PBS and fixed with 2% paraformaldehyde. Fixed cells were blocked with 20% skim milk, incubated with AF647-conjugated donkey anti-rat IgG and AF488-conjugated donkey anti-rabbit IgG secondary antibodies (1:200) at room temperature for 1 h, washed 3 times with PBS, and mounted for imaging. For immunofluorescence on permeabilized cells, cells were fixed with 2% paraformaldehyde, permeabilized with chilled methanol, blocked with 20% skim milk, and then incubated with primary and secondary antibodies.

ELISA of surfactant protein C (SPC) and ATP measurement

Mouse SPC ELISA Kit (ab252366, Abcam) and ATP Determination Kit (S0026, Beyotime) were used to detect the concentrations of mature SPC and ATP in bronchoalveolar lavage fluid of the mice, respectively. The procedures were according to the manufactures' instructions.

Determination of DPPC

The standard of DPPC (1,2-dipalmitoyl-sn-glycero-3-phosphocholine) was purchased from Avanti polar lipids (Cat #850355). The HPLC-grade methanol, chloroform, 2-isopropanol and acetonitrile were purchased from Sigma-Aldrich (USA), and the ammonium acetate was purchased from Mallinckrodt Baker, Inc. (Phillipsburg, NJ).

The lavage fluid was conducted directly to liquid chromatography/tandem mass spectrometry (LC-MS/MS, QTRAP 5500+, AB Sciex, Canada) for DPPC determination. LC separation was performed on a Kinetex[®] C18 column (2.6 μ m, 100 \times 2.1 mm 100Å, Phenomenex), at a flow rate of 0.45 mL/min and a column temperature of 40 °C with a loading volume of 2 μ l. The mobile phase consisted of mobile phase A (water: methanol: acetonitrile=1:1:1, 7 mM ammonium acetate), and mobile phase B (2-isopropanol, 7 mM ammonium acetate). The eluted condition: 0-0.8 min 50% B; 0.8-4.80 min 50%-80% B; 4.80-4.90 min 80%-98% B; 4.90-5.50 min 98%-50% B; 5.50-6.30 min 50% B. DPPC eluted at 2.84 min and the quantification were carried out under MRM (multiple reaction monitor) mode with m/z at 734.6 (Q1) and 184.3 (Q3) in positive mode through LC-MS/MS. DP and CE values were 100 and 35, respectively.

Intratracheal instillation of AAV into mouse lungs

The mouse was anesthetized with isoflurane and an endotracheal cannula was inserted into the trachea. AAV was infused into the lung by using a manually pulled long and thin micropipette tip through the endotracheal cannula. Mechanical ventilation was performed for 5 min after instillation. Anesthetization is terminated when the mouse recovered spontaneous breathing of normal rhythm in ~10 min. Then the mouse was returned to its home cage.

An AAV6-based triple mutant capsid (AAV6.2FF)(65) was employed to deliver transgenes into mouse lungs. AAV dosage/mouse: 50 μ l CMV-h63B-3xFlag-tWPA (2.27×10^{12} v.g./ml), 25 μ l CMV-h63A-3xFlag-tWPA (9.26×10^{12} v.g./ml), 25 μ l CMV-MCS(Ctrl)-3xFlag-tWPA (8.95×10^{12} v.g./ml), 50 μ l CMV-h63B-Y572A-3xFlag-tWPA

(3.34×10^{12} v.g./ml) and 25 μ l CAG-DIO-jGCaMP7s-mCherry-WPRE (6.23×10^{12} v.g./ml). Instillation of AAV was performed at 12-16 h after the first injection of tamoxifen.

Genome editing in mouse lungs

The AAV U6-spgRNA(*Tmem63b*)-donor(V5tag)-WPRE, which carries the gRNA sequence “GGCCAGCAAGAACGGCAGCA” that targets the start codon region of mouse *Tmem63b* gene and 2×V5 tag sequence with 400-bp homology arms on both sides, was instilled into the lungs of SpCas9-transgenic mice (50 μ l/mouse, 9.06×10^{12} v.g./ml). After 3 weeks the lungs were dissected and frozen sectioned for immunofluorescence.

ATP/saline inhalation

Ager-Sftpc-63ab, Sftpc-63ab and Ctrl-63ab mice were injected with tamoxifen for 5 consecutive days. From the next day after the last tamoxifen injection, the mice were placed in an anesthesia induction chamber, in which aerosolized Na₂ATP solution (200 mM) or saline was provided by connecting to a nebulizer. Aerosol inhalation was conducted 0.5 h each time, 3 times/day until the cDKO mice died.

Mechanical strain of AT2 cells

To examine Ca²⁺ response directly induced by mechanical strain, AT2 cells were grown on fibronectin-coated silicone membrane (~12 mm in diameter, 0.1 mm thickness, transparent) firmly adhered to the glass of a glass-bottom dish. The cells were stained with 5 μ M Fluo-4 AM in culture medium for 20 min, which was then changed to physiological extracellular solution for Ca²⁺ imaging. A glass micropipette was moved toward the cell in the same way for patch clamp with a micromanipulator. The tip of the micropipette was then pierced into the silicone membrane close to the cell. Time-lapse imaging for fluo-4 fluorescence was started with exposure time of 100 ms and no interval. The micropipette tip was moved horizontally for 20 μ m away from the cell and returned its original position during imaging. Fluorescent intensity of each cell was

measured from images at different time points.

For strain-induced surfactant release experiment, a custom strain chamber with silicone membrane (10 cm × 10 cm, 0.1 mm thickness) stretched by cyclic vacuum pressure from an electric breast pump was used. AT2 cells were grown on the center of fibronectin-coated silicone membrane and subject to cyclic strain or static culture. The silicone membrane was then removed from the chamber and mounted on the microscope to capture high-resolution images of AT2 cells for LB counting.

To observe LBs in the same AT2 cell before and after strain, the silicone membrane was directly mounted on the 100× objective after ATP treatment and FM4-64 staining. After taking image for an individual cell, a blunted glass micropipette driven by a micromanipulator was used to stretch the cell by pressing its adjacent silicone membrane area with an angle of ~45°, distance of 200 μm and frequency of 1 Hz. After strain for 5 min and 10 min, the cell was refocused and imaged if it was not detached.

Transmission electron microscopy

Transmission Electron microscopy was performed in Lilai Biomedical Experimental Center (Chengdu, China). Fresh lung samples of ~1 mm thickness were prefixed with 3% glutaraldehyde, and then postfixed in 1% osmium tetroxide, dehydrated in series acetone, infiltrated in Epox 812 and embedded. The semithin sections were stained with methylene blue. Ultrathin sections were produced by cutting with diamond knife, and stained with uranyl acetate and lead citrate. The sections were examined with JEM-1400-FLASH Transmission Electron Microscope (JEOL, Japan).

Statistics

Data are presented as mean ± SEM (standard error of mean) unless otherwise mentioned. In violin plot, median and quartiles are shown in the graph. Student's *t* test was used in experiment with only two groups. One-way ANOVA and Tukey's test were used to identify statistical differences among 3 or more groups. Two-way ANOVA and Sidak's test were employed when the response was affected by two factors (time and drug treatment). Statistical results are indicated by ns (nonsignificant), **P*<0.05, ***P*<0.01,

*** $P < 0.001$ and **** $P < 0.0001$.

Study approval

All the animal experimental procedures were reviewed and approved by the Ethical Committee of Southwest Medical University and in accordance with the national guidelines for housing and use of laboratory animals.

Human AT2 cells were isolated from normal lung tissues cut off with tumors from patients (one male and one female) undergoing lung cancer surgery. Isolated cells were used for Ca^{2+} imaging and patch clamp. The experiment using human lung samples was approved by the Ethical Committee of Southwest Medical University. Informed consent was obtained from all subjects.

Data availability

Data generated in this study are available from the “Supporting data values” file or the corresponding author upon reasonable request.

ACKNOWLEDGEMENTS

This study was supported by National Natural Science Foundation of China (81974093 and 32171106), Sichuan Science and Technology Program (2022YFS0627 and 2022YFS0607), and Natural Science Foundation of Sichuan Province (2022NSFSC0703).

AUTHOR CONTRIBUTIONS

Study design, supervision and manuscript preparation: G.-L.C. and B.Z.; Histology and microscopic imaging: J.-Y.Li, J.-W.L., Q.Z., J.-Y.Liu and B.Z.; Patch clamp: G.-L.C., J.-Y.Li, X.C., J.-Y.Liu, J.W. and N.W.; Animal experiments: G.-L.C., J.-Y.Li, Q.Z., J.-Y.Liu, J.W., J.-P.W., L.Y. and Y.-P.L.; Molecular cloning and mutagenesis: J.-W.L. and J.J.L.; Primary cell culture: X.C., M.L. and H.-Q.Y.; Genome editing: G.-L.C. and B.Z.; LC-MS/MS: Z.H. and J.D.; Structural modeling: J.Z.. The order of co-first authors were assigned based on the academic contribution of individual authors.

CONFLICT OF INTEREST

The authors declare that there are no conflicts of interest.

REFERENCES

1. Clements JA, and Avery ME. Lung surfactant and neonatal respiratory distress syndrome. *Am J Respir Crit Care Med.* 1998;157(4 Pt 2):S59-66.
2. Hite RD. Surfactant Deficiency in Adults. *Clinical Pulmonary Medicine.* 2002;9(1):39-45.
3. Grygorczyk R, et al. Mechanosensitive ATP release in the lungs: New insights from real-time luminescence imaging studies. *Curr Top Membr.* 2019;83:45-76.
4. Dietl P, et al. Spatio-temporal aspects, pathways and actions of Ca(2+) in surfactant secreting pulmonary alveolar type II pneumocytes. *Cell Calcium.* 2012;52(3-4):296-302.
5. Fois G, et al. ATP is stored in lamellar bodies to activate vesicular P2X4 in an autocrine fashion upon exocytosis. *J Gen Physiol.* 2018;150(2):277-291.
6. Patel AS, et al. Paracrine stimulation of surfactant secretion by extracellular ATP in response to mechanical deformation. *Am J Physiol Lung Cell Mol Physiol.* 2005;289(3):L489-496.
7. Tan JJ, et al. Type 2 secretory cells are primary source of ATP release in mechanically stretched lung alveolar cells. *Am J Physiol Lung Cell Mol Physiol.* 2020;318(1):L49-L58.
8. Singer W, et al. Mechanical forces impeding exocytotic surfactant release revealed by optical tweezers. *Biophys J.* 2003;84(2 Pt 1):1344-1351.
9. Douguet D, and Honore E. Mammalian Mechano-electrical Transduction: Structure and Function of Force-Gated Ion Channels. *Cell.* 2019;179(2):340-354.
10. Kefauver JM, et al. Discoveries in structure and physiology of mechanically activated ion channels. *Nature.* 2020;587(7835):567-576.
11. Zheng W, et al. TMEM63 proteins function as monomeric high-threshold mechanosensitive ion channels. *Neuron.* 2023;111(20):3195-3210 e3197.
12. Diem K, et al. Mechanical stretch activates piezo1 in caveolae of alveolar type I cells to trigger ATP release and paracrine stimulation of surfactant secretion from alveolar type II cells. *FASEB J.* 2020;34(9):12785-12804.
13. Li X, et al. Generation of Piezo1-CreER transgenic mice for visualization and lineage tracing of mechanical force responsive cells in vivo. *Genesis.* 2022;60(4-5):e23476.
14. Lee LM, et al. Pathophysiological Role of K(2P) Channels in Human Diseases. *Cell Physiol Biochem.* 2021;55(S3):65-86.
15. Zheng W, and Holt JR. The Mechanosensory Transduction Machinery in Inner Ear Hair Cells. *Annu Rev Biophys.* 2021;50:31-51.
16. Zhang M, et al. Structure of the mechanosensitive OSCA channels. *Nat Struct Mol Biol.* 2018;25(9):850-858.
17. Murthy SE, et al. OSCA/TMEM63 are an Evolutionarily Conserved Family of Mechanically Activated Ion Channels. *Elife.* 2018;7:e41844.
18. Du H, et al. The Cation Channel TMEM63B Is an Osmosensor Required for Hearing. *Cell Rep.* 2020;31(5):107596.
19. Dong TX, et al. T-cell calcium dynamics visualized in a ratiometric tdTomato-GCaMP6f transgenic reporter mouse. *Elife.* 2017;6.
20. Rice WR, and Singleton FM. P2Y-purinoreceptor regulation of surfactant secretion from rat isolated alveolar type II cells is associated with mobilization of intracellular calcium. *Br J Pharmacol.* 1987;91(4):833-838.
21. Rice WR, et al. P2-purinoreceptor regulation of surfactant phosphatidylcholine secretion.

876 Relative roles of calcium and protein kinase C. *Biochem J*. 1990;266(2):407-413.

877 22. Hohenegger M, et al. Activation of the skeletal muscle ryanodine receptor by suramin and
878 suramin analogs. *Mol Pharmacol*. 1996;50(6):1443-1453.

879 23. Pulcinelli FM, et al. Evidence for separate effects of U73122 on phospholipase C and
880 calcium channels in human platelets. *Biochem Pharmacol*. 1998;56(11):1481-1484.

881 24. Wirsching E, et al. P2 Purinergic Signaling in the Distal Lung in Health and Disease. *Int J*
882 *Mol Sci*. 2020;21(14):4973.

883 25. Kato Y, et al. Identification of a vesicular ATP release inhibitor for the treatment of
884 neuropathic and inflammatory pain. *Proc Natl Acad Sci U S A*. 2017;114(31):E6297-E6305.

885 26. DeCoursey TE. Hypothesis: do voltage-gated H(+) channels in alveolar epithelial cells
886 contribute to CO(2) elimination by the lung? *Am J Physiol Cell Physiol*. 2000;278(1):C1-
887 C10.

888 27. Matalon S, et al. Invited review: biophysical properties of sodium channels in lung alveolar
889 epithelial cells. *J Appl Physiol (1985)*. 2002;93(5):1852-1859.

890 28. Schmitz G, and Muller G. Structure and function of lamellar bodies, lipid-protein
891 complexes involved in storage and secretion of cellular lipids. *J Lipid Res*.
892 1991;32(10):1539-1570.

893 29. Chen CC, et al. Patch-clamp technique to characterize ion channels in enlarged individual
894 endolysosomes. *Nat Protoc*. 2017;12(8):1639-1658.

895 30. Dana H, et al. High-performance calcium sensors for imaging activity in neuronal
896 populations and microcompartments. *Nat Methods*. 2019;16(7):649-657.

897 31. Chen X, et al. TMEM63 mechanosensitive ion channels: Activation mechanisms, biological
898 functions and human genetic disorders. *Biochem Biophys Res Commun*. 2023;683:149111.

899 32. Adamson SL. Regulation of breathing at birth. *J Dev Physiol*. 1991;15(1):45-52.

900 33. Shi Y, et al. A brainstem peptide system activated at birth protects postnatal breathing.
901 *Nature*. 2021;589(7842):426-430.

902 34. Li J, et al. The Strength of Mechanical Forces Determines the Differentiation of Alveolar
903 Epithelial Cells. *Dev Cell*. 2018;44(3):297-312 e295.

904 35. Holm BA, and Matalon S. Role of pulmonary surfactant in the development and treatment
905 of adult respiratory distress syndrome. *Anesth Analg*. 1989;69(6):805-818.

906 36. Dushianthan A, et al. Pulmonary Surfactant in Adult ARDS: Current Perspectives and
907 Future Directions. *Diagnostics (Basel)*. 2023;13(18).

908 37. Anzueto A, et al. Aerosolized surfactant in adults with sepsis-induced acute respiratory
909 distress syndrome. Exosurf Acute Respiratory Distress Syndrome Sepsis Study Group. *N*
910 *Engl J Med*. 1996;334(22):1417-1421.

911 38. Spragg RG, et al. Effect of recombinant surfactant protein C-based surfactant on the acute
912 respiratory distress syndrome. *N Engl J Med*. 2004;351(9):884-892.

913 39. Raghavendran K, et al. Surfactant therapy for acute lung injury and acute respiratory
914 distress syndrome. *Crit Care Clin*. 2011;27(3):525-559.

915 40. Possmayer F, et al. Pulmonary surfactant. *Can J Biochem Cell Biol*. 1984;62(11):1121-1133.

916 41. Taruno A. ATP Release Channels. *Int J Mol Sci*. 2018;19(3):808.

917 42. Syrjanen J, et al. On the molecular nature of large-pore channels. *J Mol Biol*.
918 2021;433(17):166994.

919 43. Okada Y, et al. Molecular Identities and ATP Release Activities of Two Types of Volume-

Regulatory Anion Channels, VSOR and Maxi-Cl. *Curr Top Membr.* 2018;81:125-176.

44. Van Rooijen N, and Sanders A. Liposome mediated depletion of macrophages: mechanism of action, preparation of liposomes and applications. *J Immunol Methods.* 1994;174(1-2):83-93.

45. Wang Y, et al. The effects and mechanisms of SLC34A2 in tumorigenesis and progression of human non-small cell lung cancer. *J Biomed Sci.* 2015;22(1):52.

46. Yu Z, et al. Identification of a transporter complex responsible for the cytosolic entry of nitrogen-containing bisphosphonates. *Elife.* 2018;7.

47. Haller T, et al. Fusion pore expansion is a slow, discontinuous, and Ca^{2+} -dependent process regulating secretion from alveolar type II cells. *J Cell Biol.* 2001;155(2):279-289.

48. Miklavc P, et al. Actin coating and compression of fused secretory vesicles are essential for surfactant secretion--a role for Rho, formins and myosin II. *J Cell Sci.* 2012;125(Pt 11):2765-2774.

49. Miklavc P, et al. Actin depolymerisation and crosslinking join forces with myosin II to contract actin coats on fused secretory vesicles. *J Cell Sci.* 2015;128(6):1193-1203.

50. Miklavc P, et al. Fusion-activated Ca^{2+} entry via vesicular P2X4 receptors promotes fusion pore opening and exocytotic content release in pneumocytes. *Proc Natl Acad Sci U S A.* 2011;108(35):14503-14508.

51. van Weeren L, et al. Rab3D and actin reveal distinct lamellar body subpopulations in alveolar epithelial type II cells. *Am J Respir Cell Mol Biol.* 2004;30(3):288-295.

52. Shin W, et al. Vesicle Shrinking and Enlargement Play Opposing Roles in the Release of Exocytotic Contents. *Cell Rep.* 2020;30(2):421-431 e427.

53. Lewis AH, and Grandl J. Mechanical sensitivity of Piezo1 ion channels can be tuned by cellular membrane tension. *Elife.* 2015;4.

54. Forrest JB. The effect of changes in lung volume on the size and shape of alveoli. *J Physiol.* 1970;210(3):533-547.

55. Boyle J, 3rd, et al. Mean air space diameter, lung surface area and alveolar surface tension. *Respiration.* 1977;34(5):241-249.

56. Grieco DL, et al. Transpulmonary pressure: importance and limits. *Ann Transl Med.* 2017;5(14):285.

57. Nonomura K, et al. Piezo2 senses airway stretch and mediates lung inflation-induced apnoea. *Nature.* 2017;541(7636):176-181.

58. Yan H, et al. Heterozygous Variants in the Mechanosensitive Ion Channel TMEM63A Result in Transient Hypomyelination during Infancy. *Am J Hum Genet.* 2019;105(5):996-1004.

59. Vetro A, et al. Stretch-activated ion channel TMEM63B associates with developmental and epileptic encephalopathies and progressive neurodegeneration. *Am J Hum Genet.* 2023;110(8):1356-1376.

60. Tabara LC, et al. TMEM63C mutations cause mitochondrial morphology defects and underlie hereditary spastic paraplegia. *Brain.* 2022;145(9):3095-3107.

61. Parpaite T, et al. Patch-seq of mouse DRG neurons reveals candidate genes for specific mechanosensory functions. *Cell Rep.* 2021;37(5):109914.

62. Witherden IR, and Tetley TD. Isolation and Culture of Human Alveolar Type II Pneumocytes. *Methods Mol Med.* 2001;56:137-146.

63. Evans RJ, et al. Ionic permeability of, and divalent cation effects on, two ATP-gated cation

964 channels (P2X receptors) expressed in mammalian cells. *J Physiol.* 1996;497 (Pt 2):413-
965 422.

966 64. Zhou X, and Moore BB. Lung Section Staining and Microscopy. *Bio Protoc.* 2017;7(10).
967 65. van Lieshout LP, et al. A Novel Triple-Mutant AAV6 Capsid Induces Rapid and Potent
968 Transgene Expression in the Muscle and Respiratory Tract of Mice. *Mol Ther Methods Clin*
969 *Dev.* 2018;9:323-329.

970

Figure 1

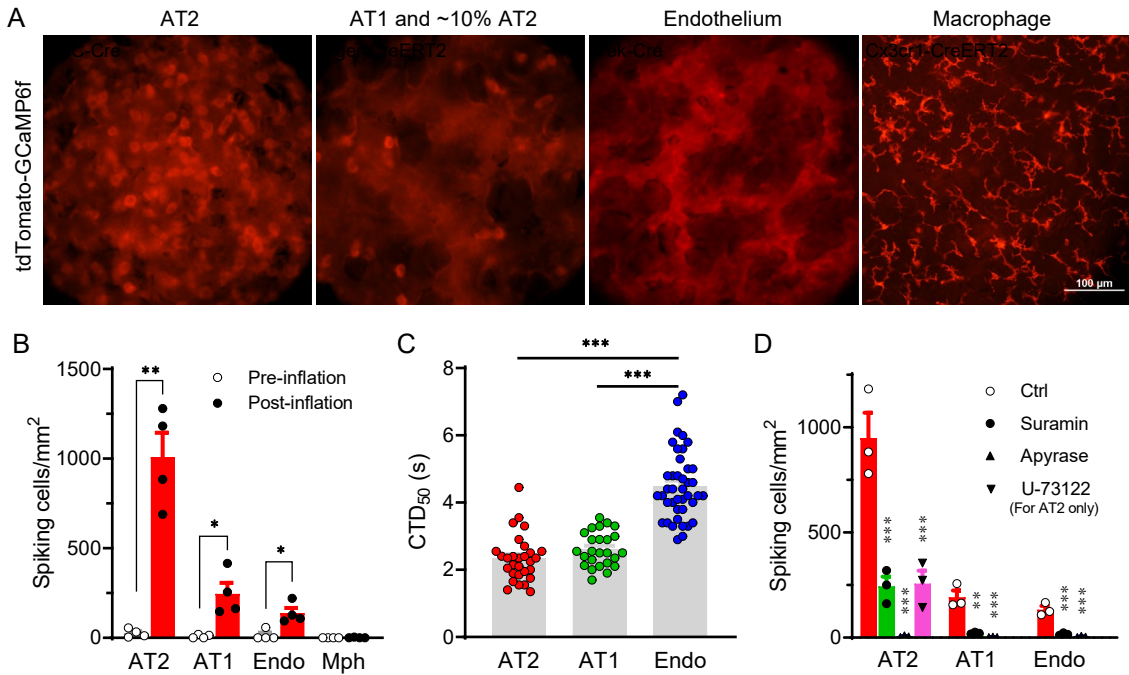


Figure 1. Mechanical ventilation-induced Ca^{2+} transients in alveolar cells of *ex vivo* mouse lungs

- (A) tdTomato fluorescence in *ex vivo* mouse lungs with Cre-driven expression of tdTomato-GCaMP6f in different cell types.
- (B) Density of cells with Ca^{2+} transients (spiking cells, indicated by sharp changes of GCaMP6f intensity) before and after mechanical ventilation with tidal volume of 200 μl for 5 min. $n=4$ lung lobes.
- (C) Duration of Ca^{2+} transients above 50% peak value (CTD₅₀). $n=29$, 25 and 41 for AT2, AT1 and endothelial cells, respectively.
- (D) Density of spiking cells in lungs intratracheally instilled with 100 μl vehicle (0.2% DMSO), suramin (300 μM ; blocking P2X and P2Y receptors), apyrase (10 U/ml; hydrolyzing ATP) or U-73122 (20 μM ; inhibiting P2Y-G_q-PLC-IP₃R pathway), and ventilated with tidal volume of 200 μl for 5 min. $n=3$ lung lobes.

* $P<0.05$, ** $P<0.01$ and *** $P<0.001$ by unpaired t test (B), or one-way ANOVA and Tukey's test (C and D).

Figure 2

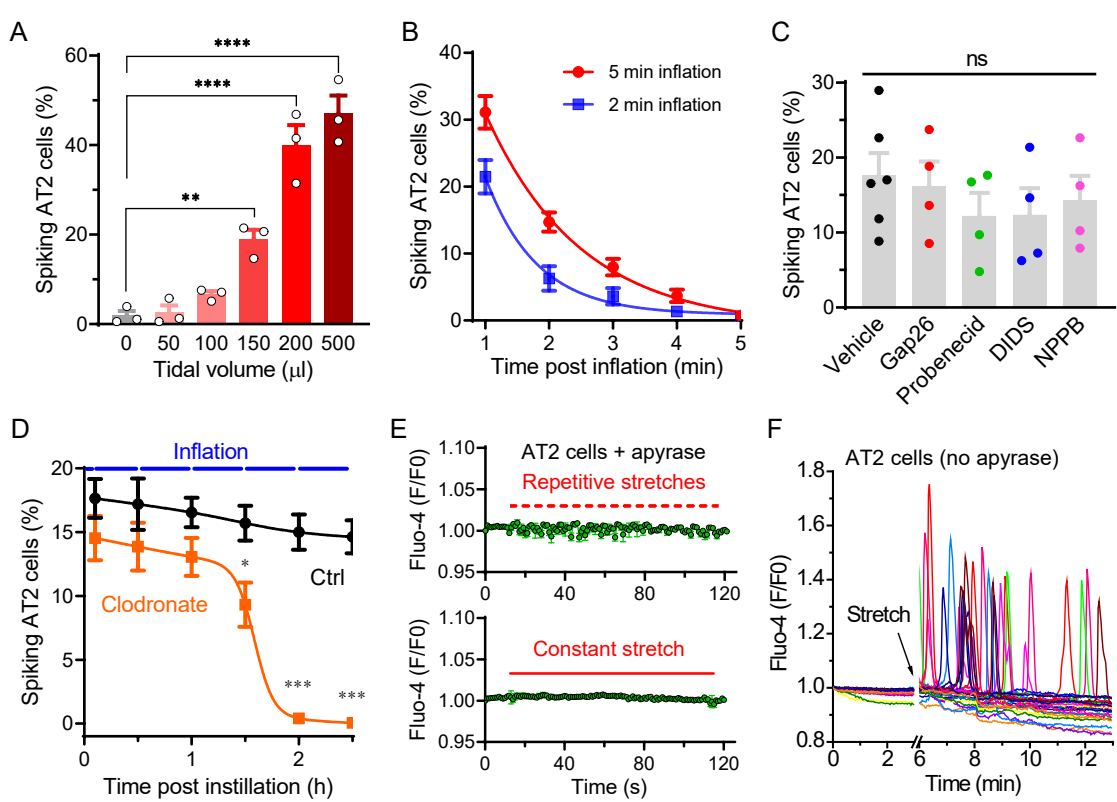


Figure 2. Properties of lung inflation and stretch-induced Ca^{2+} transients in AT2 cells

(A) Density of spiking AT2 cells in lungs ventilated with different tidal volumes for 5 min. The number of GCaMP6f-spiking cells was divided by the number of tdTomato⁺ cells (i.e. total number of AT2 cells) in the same area to calculate the percentage. $n=3$ lung lobes. ** $P<0.01$ and **** $P<0.0001$ by one-way ANOVA and Tukey's test.

(B) Rapid decay of the density of spiking AT2 cells after ventilation with tidal volume of 200 μl for 2 and 5 min, respectively. Data were fitted with a single exponential decay function. $n=5$ lung lobes.

(C) Percent of spiking AT2 cells in lungs instilled with 150 μl vehicle (0.1% DMSO), Cx43 blocker Gap26 (500 μM), pannexin blocker probenecid (2 mM), Cl^- channel blocker DIDS (200 μM) or NPPB (100 μM) after ventilation with tidal volume of 150 μl for 5 min. $n=6$ (vehicle) and 4 (others) lung lobes; ns, nonsignificant by one-way ANOVA.

(D) Percent of spiking AT2 cells in lungs instilled with 150 μl clodronate (100 μM) or Ctrl solution. The data were fitted with a biphasic dose-response curve (corresponding to abundance of ATP-containing LBs). $n=6$ lung lobes. * $P<0.05$ and *** $P<0.001$ by two-way ANOVA and Sidak's test.

(E) Lack of direct stretch-activated Ca^{2+} response in primary AT2 cells cultured on elastic membrane. Apyrase (10 U/ml) was used to eliminate ATP released into extracellular space. $n=12$ cells.

(F) Stretch-induced ATP-mediated Ca^{2+} oscillations in primary AT2 cells. Each trace represents fluorescence of an AT2 cell. $n=26$ cells.

Figure 3

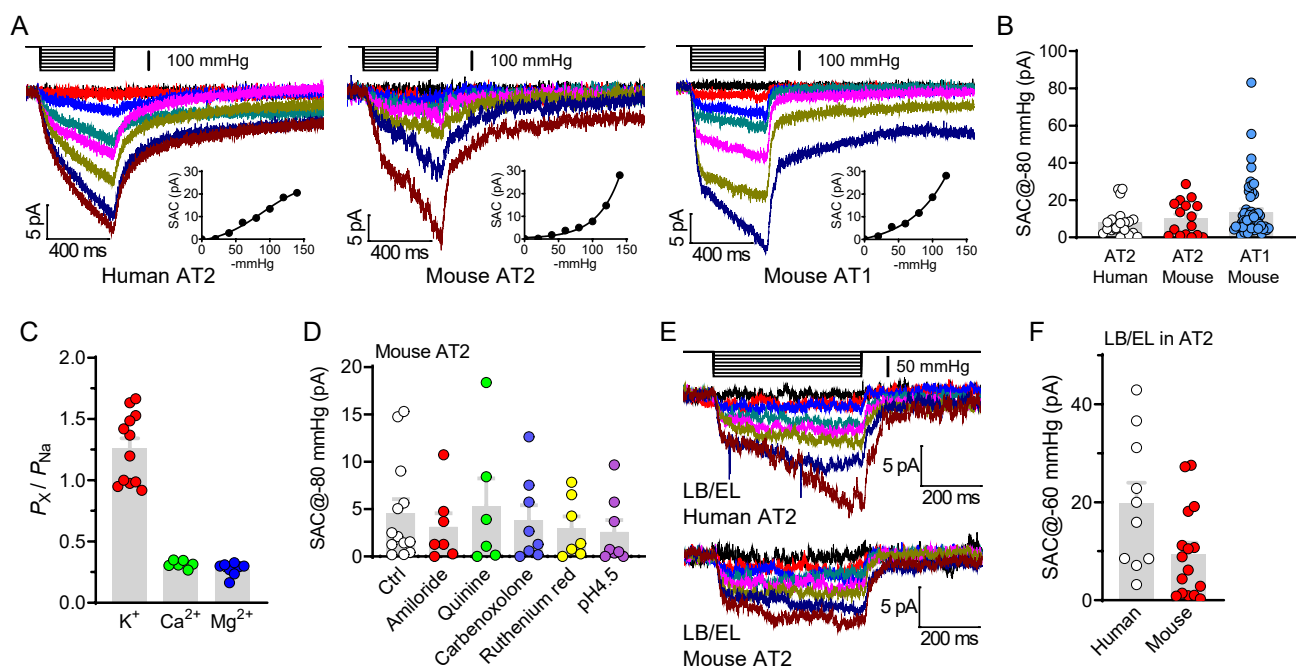


Figure 3. Mechanosensitive currents in human and mouse AECs

(A) Stretch-activated currents (SACs) under cell-attached configuration in primary human and mouse AT2 cells, and mouse AT1 cells in acute lung slices. The holding potential was -80 mV and the vacuum pressures were applied to the clamped membrane with -20 mmHg increase for each step. Insets are pressure-current relationships of corresponding recordings.

(B) The amplitudes of SACs induced by -80 mmHg pressure in human/mouse AT2 and mouse AT1 cells. $n=20$, 16 and 56 for human AT2, mouse AT2 and mouse AT1 cells, respectively.

(C) Relative permeability of K^+ , Ca^{2+} and Mg^{2+} vs Na^+ for stretch-activated currents in mouse AT2 cells. $n=12$, 6 and 8 cells for K^+ , Ca^{2+} and Mg^{2+} , respectively.

(D) Non-selective blockers of ENaC (amiloride, 10 μ M), K^+ channels (quinine, 500 μ M), gap junctions (carbenoxolone, 100 μ M) and Piezo1 (ruthenium red, 50 μ M), and acidic pH did not affect the stretch-activated currents in mouse AT2 cells. $n=13$, 7, 6, 8, 7 and 8 cells from left to right.

(E) SACs under vesicle-attached configuration in enlarged lamellar bodies and endolysosomes (LB/EL) from mouse AT2 cells. The holding potential was -60 mV and the vacuum pressures were applied with -10 mmHg increase for each step.

(F) Comparison of the amplitudes of stretch-activated currents from LB/EL. $n=10$ and 16 cells from human and mouse, respectively.

Figure 4

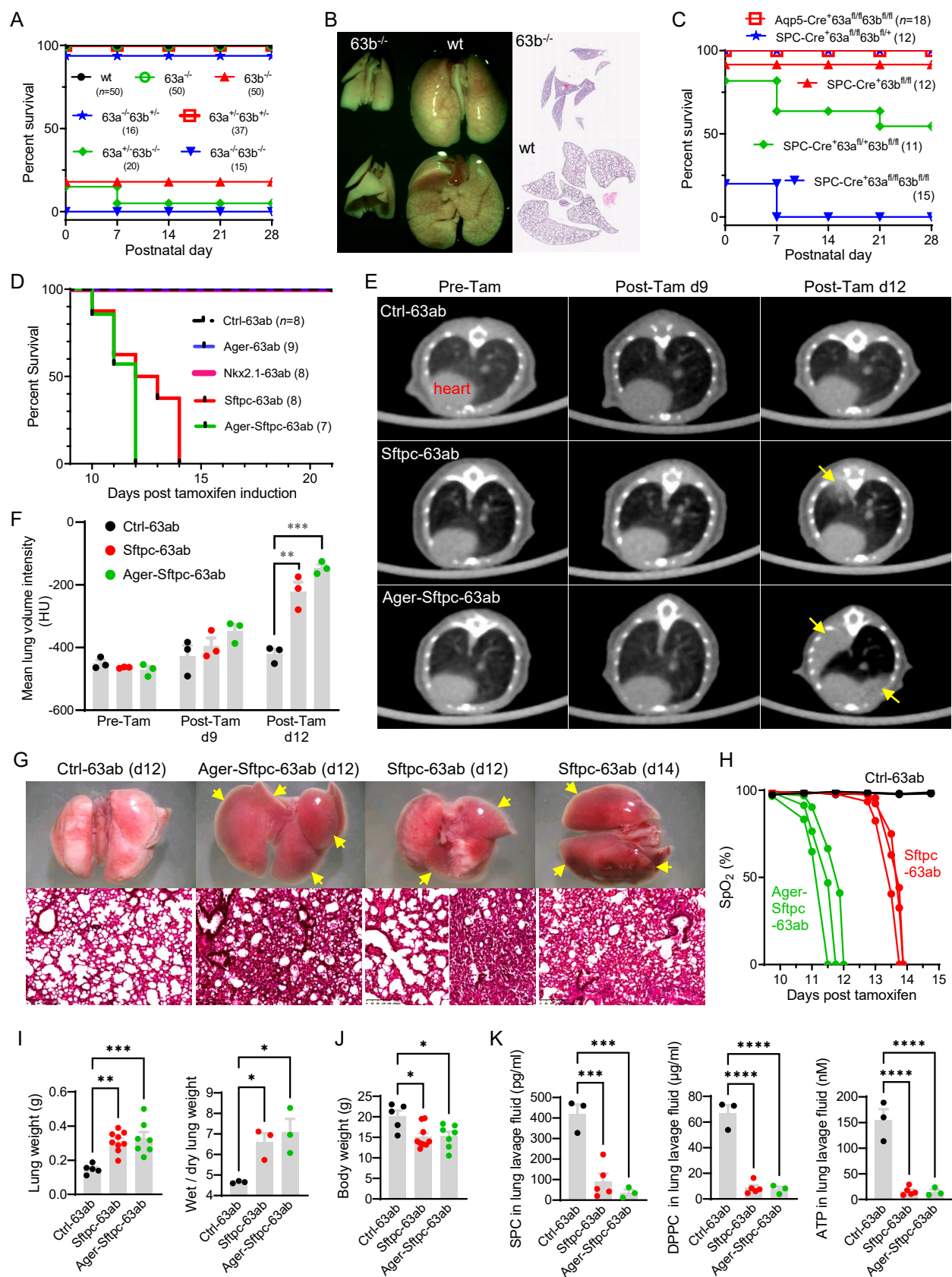


Figure 4. Lethal pulmonary phenotypes of TMEM63A/B knockout mice

- (A) Survival curves of constitutive *Tmem63a/b* knockout mice with different genotypes. The *n* numbers of mice are shown in parentheses.
- (B) Failure of alveolar expansion in *Tmem63b* knockout mice after birth (P0).
- (C) Survival curves of AEC-specific *Tmem63a/b* conditional knockout mice with different genotypes. Aqp5-Cre is expressed in AT1 and ~50% AT2 cells. SPC-Cre is expressed in all AT2 cells.
- (D) Survival curves of tamoxifen-inducible AEC-specific *Tmem63a/b* conditional double knockout (cDKO) mice. Ager-CreERT2: AT1 and ~10% AT2; Nkx2.1-CreERT2: AT1 and ~80% AT2. Sftpc-CreERT2: all AT2. Ctrl-63ab represents 63a^{fl/fl}63b^{fl/fl} without Cre, and others are with corresponding CreERT2.
- (E) Micro-computed tomography (microCT) images of mouse lungs after tamoxifen induction. Arrows indicate regions of atelectasis.
- (F) Mean lung volume intensities of the mice before and after tamoxifen induction measured from microCT. *n*=3 mice.
- (G) Atelectasis in cDKO mice illustrated by freshly dissected lungs and HE-stained sections. Arrows indicate collapsed lobes.
- (H) Dramatic decline of saturation of peripheral oxygen (SpO₂) before respiratory failure in cDKO mice. *n*=3 mice.
- (I) Characteristics of pulmonary edema in cDKO mice at Post-Tam d12. *n*=5, 9 and 7 mice for lung weight from left to right and *n*=3 mice for wet/dry ratio.
- (J) Body weights in cDKO mice at Post-Tam d12. *n*=5, 9 and 7 mice from left to right.
- (K) Deficiency of secreted surfactant protein C (SPC), surfactant phospholipid DPPC and ATP in bronchoalveolar lavage fluid collected from cDKO mice at Post-Tam d10. *n*=3, 5 and 3 mice from left to right in each graph.

P*<0.05, *P*<0.01, ****P*<0.001 and *****P*<0.0001 by one-way ANOVA and Tukey's test.

Figure 5

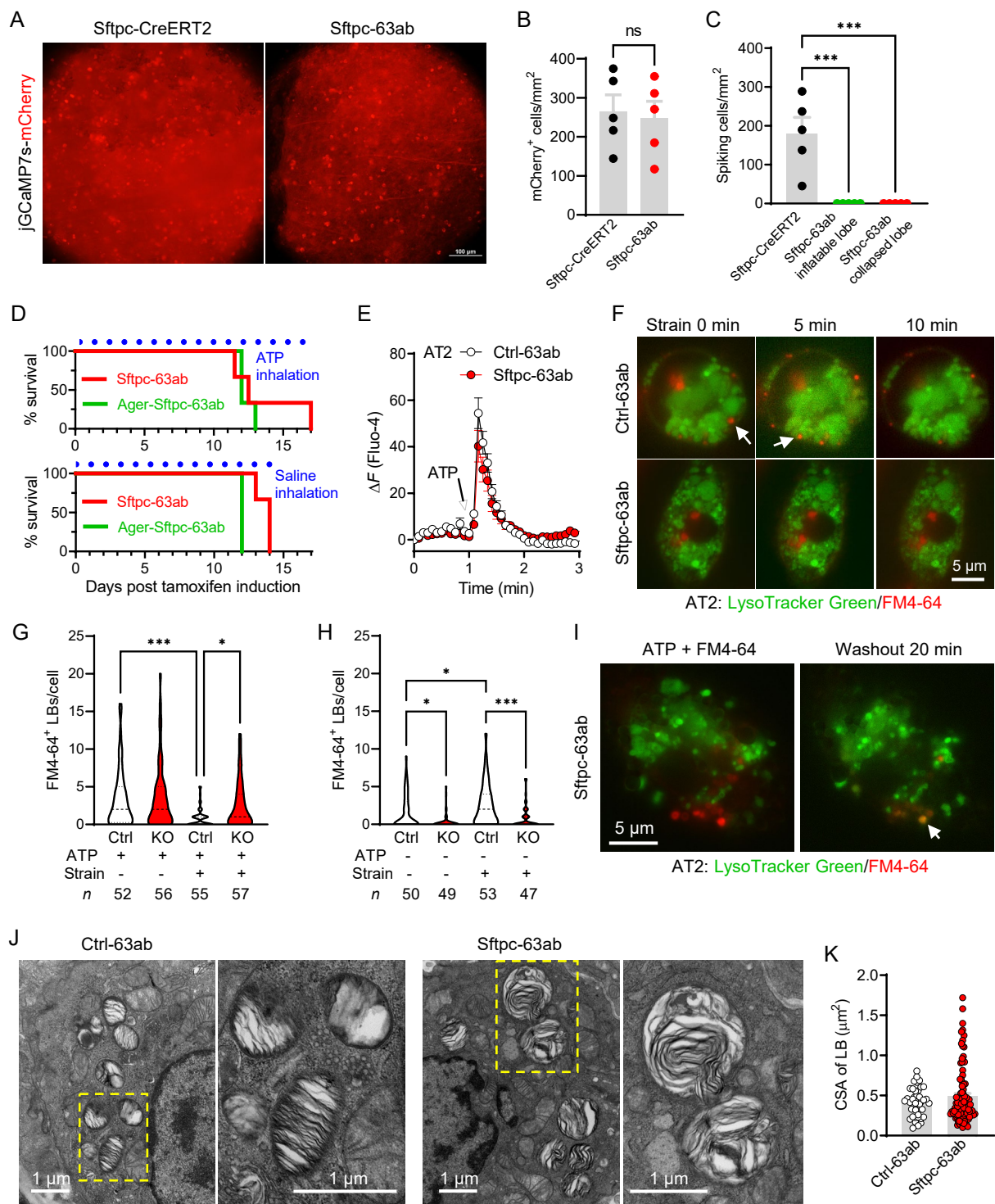


Figure 5. Deficiency of TMEM63A/B abolished ventilation-induced Ca^{2+} transients and surfactant release in AT2 cells

- (A) mCherry fluorescence in AAV (CAG-DIO-jGCaMP7s-mCherry)-infected lungs showing positively transduced AT2 cells (brighter spots). Sftpc-63ab represents Sftpc-CreERT2^{+/-}63a^{fl/fl}63b^{fl/fl}.
- (B) The densities of positively transduced AT2 cells are comparable between the control Sftpc-CreERT2 and Sftpc-63ab mice. $n=5$ lung lobes; ns, nonsignificant by unpaired t test.
- (C) Lung inflation-induced Ca^{2+} transients in AT2 cells were completely abolished in all lung lobes from Sftpc-63ab mice, revealed by jGCaMP7s fluorescence. $n=5$ lung lobes; *** $P<0.001$ by one-way ANOVA and Tukey's test.
- (D) Survival curves of *Tmem63a/b* cDKO mice received daily inhalation (30 min each time, 3 times/day) of aerosolized ATP (200 mM) or saline solution after tamoxifen induction. $n=3$ mice.
- (E) ATP-induced Ca^{2+} response in primary AT2 cells isolated from Ctrl-63ab (63a^{fl/fl}63b^{fl/fl}) and Sftpc-63ab mice ($n=30$ and 35 cells, respectively).
- (F) Cell strain-induced surfactant release occurred in AT2 cells from Ctrl-63ab but not Sftpc-63ab mice. Unfused LBs are stained by LysoTracker Green; LBs fused on the plasma membrane are positive for FM4-64. Arrows indicate LBs that released surfactant (FM4-64 fluorescence disappeared after strain).
- (G) and (H) *Tmem63a/b* cDKO did not affect ATP-induced LB fusion, but significantly attenuated cell strain-induced surfactant release. Ctrl: Ctrl-63ab; KO: Sftpc-63ab. Median and quartiles are shown by dashed and dotted lines, respectively. The n numbers of cells are shown at the bottom; * $P<0.05$, *** $P<0.001$ by one-way ANOVA and Tukey's test.
- (I) Reacidification of lamellar bodies after removal of ATP in AT2 cells from Sftpc-63ab mice. Overlapped LysoTracker Green and FM4-64 fluorescence (orange, indicated by the arrow) suggest that the fusion pore is closed and luminal pH is reacidified.
- (J) and (K), Transmission electron microscopy images and cross-sectional areas (CSA) of LBs from Ctrl-63ab and Sftpc-63ab mice ($n=41$ and 94 LBs, respectively).

Figure 6

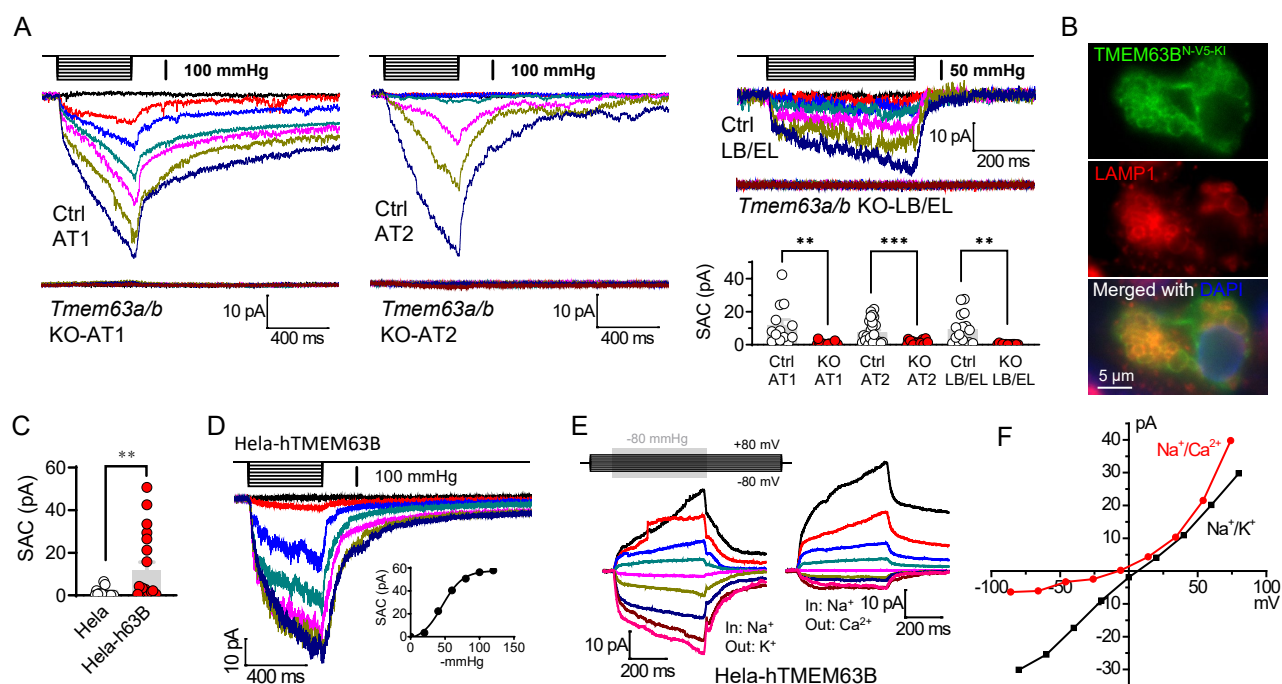


Figure 6. TMEM63A/B are essential for mechanosensitive currents in AECs

- (A) Stretch-activated currents (SACs) were abolished in AT1, AT2 and LB/EL from *Tmem63a/b* cDKO mice. Current amplitudes at -80 mV and -80 mmHg for AT1 and AT2 cells, and -60 mV and -60 mmHg for LB/EL were used for comparison. $n=13$ (Ctrl-AT1, from Ctrl-63ab mice), 18 (KO-AT1, from Ager-63ab), 25 (Ctrl-AT2, from Ctrl-63ab), 21 (KO-AT2, from Sftpc-63ab), 16 (Ctrl-LB/EL, from Ctrl-63ab) and 13 (KO-LB/EL, from Sftpc-63ab) cells. ** $P < 0.01$ and *** $P < 0.001$ by unpaired t test.
- (B) Immunofluorescence of endogenous TMEM63B with N terminal 2 \times V5-tag knock-in (N-V5-KI) in an AT2 cell in the frozen section of mouse lung. LAMP1 is a marker of lamellar bodies.
- (C) Amplitudes of SACs in control and human TMEM63B (h63B)-transfected Hela cells. Holding potential: -80 mV; pressure: -80 mmHg. $n=18$ and 20 cells for Hela and Hela-h63B, respectively. ** $P < 0.01$ by unpaired t test.
- (D) Representative traces of SACs under cell-attached configuration in a h63B-transfected Hela cell. The pressure-current relationship is inset.
- (E) and (F), SAC traces and current-voltage relationships of inside-out recordings from h63B-transfected Hela cells suggesting selectivity for Na⁺ and K⁺ over Ca²⁺.

Figure 7

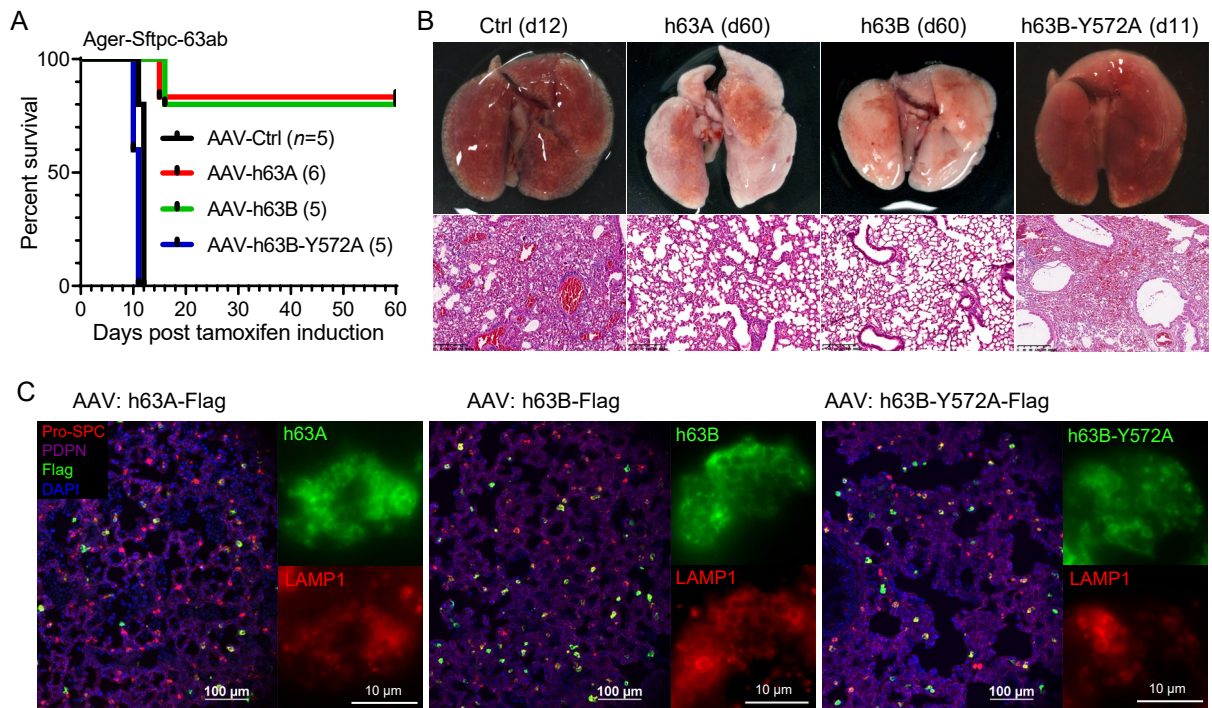


Figure 7. Human TMEM63A/B rescued respiratory failure in *Tmem63a/b* cDKO mice

- (A) Survival curves of Ager-Sftpc-63ab cDKO mice received intratracheally delivered AAVs with empty vector (Ctrl), human TMEM63A (h63A), human TMEM63B (h63B) or h63B-Y572A mutant after tamoxifen induction. The *n* numbers of mice are shown in parentheses.
- (B) Relatively normal appearance and structure of h63A and h63B-rescued lungs comparing with the lungs transduced with Ctrl or h63B-Y572A AAV.
- (C) Expression of h63A, h63B and h63B-Y572A in mouse lungs and localization in AT2 cells. Immunofluorescence against Pro-SPC (AT2), PDPN (AT1), Flag (h63A/B) and LAMP1 (LBs) are shown.